J. Fluid Mech. (1982), *vol.* 120, *pp.* 155–183
Printed in Great Britain

Development of mixing and isotropy in inviscid homogeneous turbulence

By JON LEE

Flight Dynamics Laboratory,
Wright-Patterson AFB, Ohio 43322, U.S.A.

(Received 29 January 1980 and in revised form 30 November 1981)

We have investigated a sequence of dynamical systems corresponding to spherical truncations of the incompressible three-dimensional Navier–Stokes equations in Fourier space. For lower-order truncated systems up to the spherical truncation of wavenumber radius 4, it is concluded that the inviscid Navier–Stokes system will develop mixing (and *a fortiori* ergodicity) on the constant energy–helicity surface, and also isotropy of the covariance spectral tensor. This conclusion is, however, drawn not directly from the mixing definition but from the observation that one cannot evolve the trajectory numerically much beyond several characteristic correlation times of the smallest eddy owing to the accumulation of round-off errors. The limited evolution time is a manifestation of trajectory instability (exponential orbit separation) which underlies not only mixing, but also the stronger dynamical characterization of positive Kolmogorov entropy (K-system).

1. Introduction

In a homogeneous field with no mean motion, the nonlinear term of the incompressible Navier–Stokes equations can be decomposed into enumerable triad interactions over infinitely coupled triad wavevectors (§ 2). By singling out a typical triad interaction it was found (Lee 1979) that its dynamical system in the absence of viscosity, called the fundamental triad-interaction system, cannot be ergodic, let alone mixing, on the constant energy–helicity surface, nor will it develop isotropy of the covariance spectral tensor after a long evolution time. This was then attributed to the existence of extraneous constants of motion besides energy and helicity. Surprisingly, some of them are not strictly invariant, yet they can restrict the trajectory flow just as the true constants of motion. Based on an earlier result (Lee 1975), it was conjectured that more and more triad interactions added to the dynamical system would annihilate the extraneous constants of motion, thereby engendering mixing in phase space. In this paper, we shall follow through this conjecture by examining a sequence of dynamical systems with increasingly many triad interactions. To obtain such a sequence, the wavevector space will be truncated to retain only those wavevectors lying in a sphere of specified radius – the spherical truncation. The lowest-order truncation involves 22 triad interactions over 13 wavevectors lying in a sphere of wavenumber radius $\sqrt{3}$. We shall also examine several of the higher-order truncated systems extending up to the spherical truncation of wavenumber radius 4 (§ 3).

In the beginning, we had hoped to provide a direct numerical test for ergodicity

and mixing. However, this has proven untenable because the true trajectory cannot be computed for a sufficiently long time for such tests. Evidently, the culprit here is trajectory instability, whereby the two initially nearby trajectories break away from each other exponentially after a short threshold time. Unfortunately, a numerical consequence is the accumulation of round-off errors, which then impedes trajectory computation over a time period longer than several characteristic correlation times of the smallest eddy. The trajectory instability can best be quantified by an effective evolution time, beyond which one can no longer guarantee the accuracy of trajectory computation. This has been suggested by the two extremes. The effective evolution time is practically infinite in the absence of trajectory instability, whereas it is in the order of a typical characteristic correlation time when the system is mixing. Theoretically speaking, trajectory instability is exhibited by K-systems; hence it is a stronger dynamical property than mixing. Similarly, mixing implies ergodicity. Finally, isotropy of the covariance spectral tensor follows from the mixing property (§ 4).

The computability problem as manifested by trajectory instability was first reported by Birkhoff & Fisher (1959) who observed irregular evolution of the initially smooth vortex sheets modelled by discrete point vortices. Later, it reappears as the predictability or internal-error-growth problem in numerical weather forecasting (Robinson 1967; Lorenz 1969). Relevant is the more recent evidence of trajectory instability in a variety of model flow problems (McLaughlin 1976; Glaz 1977; Lee 1980). Although trajectory instability is detrimental to the numerical trajectory evolution, it is just the ingredient that we need for the statistical turbulence formulation. This is because trajectory instability engenders the loss of initial information, thereby providing a logical link between the macroscopic irreversibility and dynamic reversibility.

Numerical details of the lowest-order truncation are presented in § 6 to demonstrate the sensitive dependence upon initial conditions, random trajectory, ergodic behaviour of modal energies, isotropy of the spectral tensor, decay of autocorrelation, and positive Kolmogorov entropy. The numerical result of the present paper is this. For the lowest-order truncation the effective evolution time is 110 under the condition described in § 5. The effective evolution time then decreases monotonically with the increasing order of spherical truncation (§ 7). It is therefore concluded that the three-dimensional Navier–Stokes system develops mixing as more and more triad interactions are included.

In the absence of mean flow motion and boundary effects, the trajectory instability of the present paper is solely attributed to nonlinearity of the Navier–Stokes equations. It is what Liepmann (1979) called a dynamical instability of rapidly increasing three-dimensional perturbations, in contrast to laminar or viscous instability of the onset of turbulence.

2. Triad-interaction representation

For the homogeneous field with no mean flow, it is most convenient to Fourier-analyse the velocity field $\mathbf{U}(\mathbf{x}, t)$ in a cyclic box of side L

$$U_i(\mathbf{x}, t) = (2\pi/L)^3 \sum_{\mathbf{k} \neq 0} U_i(\mathbf{k}, t) \exp i\mathbf{k}.\mathbf{x} \quad (i = 1, 2, 3), \tag{1}$$

where the wavevector $\mathbf{k} = (2\pi/L)\mathbf{n}$ ($n_i = 0, \pm 1, \pm 2, \ldots$). The incompressible fluid

motion can be spanned by the polarization vectors $\boldsymbol{\epsilon}^{\mu}(\mathbf{k}, \xi)$ lying on a plane normal to the wavevector $\mathbf{k}$:

$$U_i(\mathbf{k}, t) = \sum_{\mu=1,\,2} \epsilon_i^{\mu}(\mathbf{k}, \xi)\, u^{\mu}(\mathbf{k}, t). \tag{2}$$

The orthonormal polarization vectors are given by (Lee 1979)

$$\boldsymbol{\epsilon}^1(\mathbf{k}, \xi) = \begin{pmatrix} -\sin\theta_k \cos\xi - \cos\theta_k \sin\eta_k \sin\xi \\ \cos\theta_k \cos\xi - \sin\theta_k \sin\eta_k \sin\xi \\ \cos\eta_k \sin\xi \end{pmatrix},$$

$$\boldsymbol{\epsilon}^2(\mathbf{k}, \xi) = \begin{pmatrix} \sin\theta_k \sin\xi - \cos\theta_k \sin\eta_k \cos\xi \\ -\cos\theta_k \sin\xi - \sin\theta_k \sin\eta_k \cos\xi \\ \cos\eta_k \cos\xi \end{pmatrix},$$

where $\cos\theta_k = k_1/k'$, $\sin\theta_k = k_2/k'$, $\cos\eta_k = k'/k$, and $\sin\eta_k = k_3/k$. Here we shall assume $k' = (k_1^2 + k_2^2)^{\frac{1}{2}}$ to be non-zero, for the zero wavevector is excluded from the expansion (1). Because of the parameter ξ, which takes on any value in $[0, 2\pi]$, the specification of $\boldsymbol{\epsilon}^{\mu}(\mathbf{k}, \xi)$ is not unique. That is, the polarization vectors may be rotated arbitrarily about the wavevector $\mathbf{k}$, as long as they lie in a plane normal to $\mathbf{k}$, which is all that is required by the orthogonality.

The flow representation by $u^{\mu}(\mathbf{k}, t)$, the triad-interaction representation, is equivalent to the vorticity form of homogeneous flow (appendix). Unlike the Fourier amplitude $U_i(\mathbf{k}, t)$ with three components ($i = 1, 2, 3$), $u^{\mu}(\mathbf{k}, t)$ has only two components ($\mu = 1, 2$); a not-insignificant reduction in the dynamical variables. The introduction of (1) and (2) into the incompressible Navier–Stokes equations in the usual manner gives the triad-interaction representation ($\mu, \lambda, \rho = 1, 2$)

$$(\partial/\partial t + \nu k^2)\, u^{\mu}(\mathbf{k}, t) = -i(2\pi/L)^{\frac{3}{2}} \sum_{\lambda,\rho} \sum_{\mathbf{k}+\mathbf{p}+\mathbf{q}=0} \overline{\phi}^{\mu|\lambda,\rho}_{\mathbf{k}|\mathbf{p},\mathbf{q}}(\xi)\, u^{\lambda *}(\mathbf{p}, t)\, u^{\rho *}(\mathbf{q}, t), \tag{3}$$

where ν is the kinematic viscosity. Here the symmetrized coupling coefficient is defined by

$$\overline{\phi}^{\mu|\lambda,\rho}_{\mathbf{k}|\mathbf{p},\mathbf{q}}(\xi) = \tfrac{1}{2}[\phi^{\mu|\lambda,\rho}_{\mathbf{k}|\mathbf{p},\mathbf{q}}(\xi) + \phi^{\mu|\rho,\lambda}_{\mathbf{k}|\mathbf{q},\mathbf{p}}(\xi)],$$

where

$$\phi^{\mu,\lambda,\rho}_{\mathbf{k}|\mathbf{p},\mathbf{q}}(\xi) = [\mathbf{k} . \epsilon^{\rho}(\mathbf{q}, \xi)]\, [\epsilon^{\mu}(\mathbf{k}, \xi) . \epsilon^{\lambda}(\mathbf{p}, \xi)].$$

The coupling coefficients over a triad wavevector satisfy the constraints necessary for energy and helicity conservations. Hence the total energy and helicity conservations are assured when arbitrarily many triad wavevectors are coupled according to the Navier–Stokes equations. In writing (3), we have used the reality requirement

$$u^{\mu *}(\mathbf{k}) = u^{\mu}(-\mathbf{k}), \tag{4}$$

which has the same form as the reality of Fourier amplitude $\mathbf{U}^*(\mathbf{k}) = \mathbf{U}(-\mathbf{k})$. To preserve (4), however, demands that the polarization vectors are unaffected by wavevector reversal

$$\boldsymbol{\epsilon}^{\mu}(\mathbf{k}, \xi) = \boldsymbol{\epsilon}^{\mu}(-\mathbf{k}, \xi).$$

Consequently, one finds that

$$\overline{\phi}^{\mu|\lambda,\rho}_{\mathbf{k}|\mathbf{p},\mathbf{q}}(\xi) = -\overline{\phi}^{\mu|\lambda,\rho}_{-\mathbf{k}|-\mathbf{p},-\mathbf{q}}(\xi).$$

Since this assures equality of the evolutions of $u^{\mu *}(\mathbf{k}, t)$ and $u^{\mu}(-\mathbf{k}, t)$ for all t, it is the dynamic reality requirement.

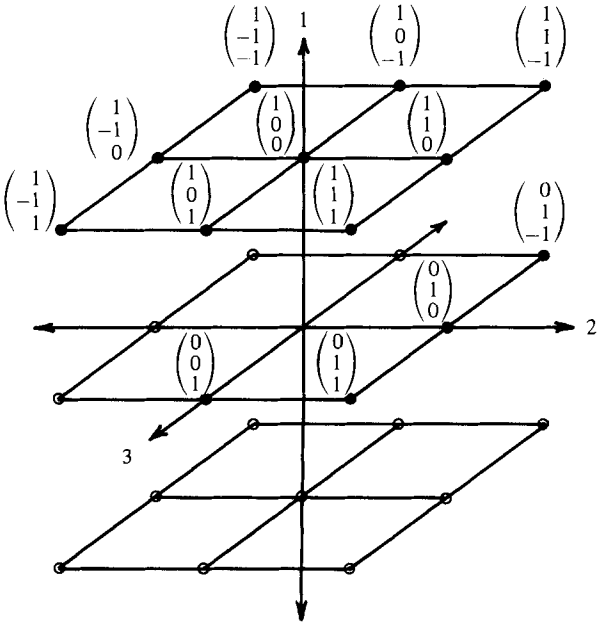

FIGURE 1. Three-dimensional wavevector lattice of $(\pm 1) \times (\pm 1) \times (\pm 1)$.

3. Lower-order systems of the spherical truncations

For definiteness, the infinite set of equations (3) must be truncated at a level appropriate for computation. To this end, let us first set $L = 2\pi$, so that $\mathbf{k} = \mathbf{n}$. In other words, the wavevectors have only the integer components and the wavevector space is now a three-dimensional lattice with integer co-ordinates. The lowest-order truncation involves the wavevector lattice of $(\pm 1) \times (\pm 1) \times (\pm 1)$ as shown in figure 1. Of the 26 wavevectors (excluding the zero vector), only a half of them need to be considered, for the remaining half are redundant due to the reality condition (4). Without loss of generality, we shall therefore choose the 13 wavevectors lying on or above the (2, 3)-plane as indicated by the solid dots in figure 1. After reordering the 13 wavevectors

$$\mathbf{k}_1 = \begin{pmatrix} 0 \\ 0 \\ 1 \end{pmatrix}, \quad \mathbf{k}_2 = \begin{pmatrix} 0 \\ 1 \\ -1 \end{pmatrix}, \quad \mathbf{k}_3 = \begin{pmatrix} 0 \\ 1 \\ 0 \end{pmatrix}, \quad \mathbf{k}_4 = \begin{pmatrix} 0 \\ 1 \\ 1 \end{pmatrix}, \quad \mathbf{k}_5 = \begin{pmatrix} 1 \\ -1 \\ 0 \end{pmatrix}, \quad \mathbf{k}_6 = \begin{pmatrix} 1 \\ 0 \\ -1 \end{pmatrix},$$

$$\mathbf{k}_7 = \begin{pmatrix} 1 \\ 0 \\ 0 \end{pmatrix}, \quad \mathbf{k}_8 = \begin{pmatrix} 1 \\ 0 \\ 1 \end{pmatrix}, \quad \mathbf{k}_9 = \begin{pmatrix} 1 \\ 1 \\ 0 \end{pmatrix}, \quad \mathbf{k}_{10} = \begin{pmatrix} 1 \\ -1 \\ -1 \end{pmatrix}, \quad \mathbf{k}_{11} = \begin{pmatrix} 1 \\ -1 \\ 1 \end{pmatrix}, \quad \mathbf{k}_{12} = \begin{pmatrix} 1 \\ 1 \\ -1 \end{pmatrix}$$

$$\mathbf{k}_{13} = \begin{pmatrix} 1 \\ 1 \\ 1 \end{pmatrix}$$

enumeration of (3) over these wavevectors gives a closed set of equations summarized in the following skeleton form:

$$\dot{\mathbf{u}}^{\mu}(\mathbf{k}, t) = -i\left\{ \begin{pmatrix} \mathbf{k}_1 \,|\, \mathbf{k}_2, -\mathbf{k}_3 \\ \mathbf{k}_2 \,|\, -\mathbf{k}_3, \mathbf{k}_1 \\ \mathbf{k}_3 \,|\, -\mathbf{k}_1, -\mathbf{k}_2 \end{pmatrix} + \begin{pmatrix} \mathbf{k}_1 \,|\, \mathbf{k}_3, -\mathbf{k}_4 \\ \mathbf{k}_3 \,|\, -\mathbf{k}_4, \mathbf{k}_1 \\ \mathbf{k}_4 \,|\, -\mathbf{k}_1, -\mathbf{k}_3 \end{pmatrix} + \begin{pmatrix} \mathbf{k}_1 \,|\, \mathbf{k}_6, -\mathbf{k}_7 \\ \mathbf{k}_6 \,|\, -\mathbf{k}_7, \mathbf{k}_1 \\ \mathbf{k}_7 \,|\, -\mathbf{k}_1, -\mathbf{k}_6 \end{pmatrix} \right.$$

$$+\begin{pmatrix}\mathbf{k}_1\,|\,\mathbf{k}_7,-\mathbf{k}_8\\ \mathbf{k}_7\,|\,-\mathbf{k}_8,\mathbf{k}_1\\ \mathbf{k}_8\,|\,-\mathbf{k}_1,-\mathbf{k}_7\end{pmatrix}+\begin{pmatrix}\mathbf{k}_1\,|\,-\mathbf{k}_5,\mathbf{k}_{10}\\ \mathbf{k}_5\,|\,-\mathbf{k}_{10},-\mathbf{k}_1\\ \mathbf{k}_{10}\,|\,\mathbf{k}_1,-\mathbf{k}_5\end{pmatrix}+\begin{pmatrix}\mathbf{k}_1\,|\,\mathbf{k}_5,-\mathbf{k}_{11}\\ \mathbf{k}_5\,|\,-\mathbf{k}_{11},\mathbf{k}_1\\ \mathbf{k}_{11}\,|\,-\mathbf{k}_1,-\mathbf{k}_5\end{pmatrix}+\begin{pmatrix}\mathbf{k}_1\,|\,-\mathbf{k}_9,\mathbf{k}_{12}\\ \mathbf{k}_9\,|\,-\mathbf{k}_{12},-\mathbf{k}_1\\ \mathbf{k}_{12}\,|\,\mathbf{k}_1,-\mathbf{k}_9\end{pmatrix}$$

$$+\begin{pmatrix}\mathbf{k}_1\,|\,\mathbf{k}_9,-\mathbf{k}_{13}\\ \mathbf{k}_9\,|\,-\mathbf{k}_{13},\mathbf{k}_1\\ \mathbf{k}_{13}\,|\,-\mathbf{k}_1,-\mathbf{k}_9\end{pmatrix}+\begin{pmatrix}\mathbf{k}_2\,|\,\mathbf{k}_5,-\mathbf{k}_6\\ \mathbf{k}_5\,|\,-\mathbf{k}_6,\mathbf{k}_2\\ \mathbf{k}_6\,|\,-\mathbf{k}_2,-\mathbf{k}_5\end{pmatrix}+\begin{pmatrix}\mathbf{k}_2\,|\,\mathbf{k}_8,-\mathbf{k}_9\\ \mathbf{k}_8\,|\,-\mathbf{k}_9,\mathbf{k}_2\\ \mathbf{k}_9\,|\,-\mathbf{k}_2,-\mathbf{k}_8\end{pmatrix}+\begin{pmatrix}\mathbf{k}_2\,|\,-\mathbf{k}_7,\mathbf{k}_{11}\\ \mathbf{k}_7\,|\,-\mathbf{k}_{11},-\mathbf{k}_2\\ \mathbf{k}_{11}\,|\,\mathbf{k}_2,-\mathbf{k}_7\end{pmatrix}$$

$$+\begin{pmatrix}\mathbf{k}_2\,|\,\mathbf{k}_7,-\mathbf{k}_{12}\\ \mathbf{k}_7\,|\,-\mathbf{k}_{12},\mathbf{k}_2\\ \mathbf{k}_{12}\,|\,-\mathbf{k}_2,-\mathbf{k}_7\end{pmatrix}+\begin{pmatrix}\mathbf{k}_3\,|\,\mathbf{k}_5,-\mathbf{k}_7\\ \mathbf{k}_5\,|\,-\mathbf{k}_7,\mathbf{k}_3\\ \mathbf{k}_7\,|\,-\mathbf{k}_3,-\mathbf{k}_5\end{pmatrix}+\begin{pmatrix}\mathbf{k}_3\,|\,\mathbf{k}_7,-\mathbf{k}_9\\ \mathbf{k}_7\,|\,-\mathbf{k}_9,\mathbf{k}_3\\ \mathbf{k}_9\,|\,-\mathbf{k}_3,-\mathbf{k}_7\end{pmatrix}+\begin{pmatrix}\mathbf{k}_3\,|\,-\mathbf{k}_6,\mathbf{k}_{10}\\ \mathbf{k}_6\,|\,-\mathbf{k}_{10},-\mathbf{k}_3\\ \mathbf{k}_{10}\,|\,\mathbf{k}_3,-\mathbf{k}_6\end{pmatrix}$$

$$+\begin{pmatrix}\mathbf{k}_3\,|\,-\mathbf{k}_8,\mathbf{k}_{11}\\ \mathbf{k}_8\,|\,-\mathbf{k}_{11},-\mathbf{k}_3\\ \mathbf{k}_{11}\,|\,\mathbf{k}_3,-\mathbf{k}_8\end{pmatrix}+\begin{pmatrix}\mathbf{k}_3\,|\,\mathbf{k}_6,-\mathbf{k}_{12}\\ \mathbf{k}_6\,|\,-\mathbf{k}_{12},\mathbf{k}_3\\ \mathbf{k}_{12}\,|\,-\mathbf{k}_3,-\mathbf{k}_6\end{pmatrix}+\begin{pmatrix}\mathbf{k}_3\,|\,\mathbf{k}_8,-\mathbf{k}_{13}\\ \mathbf{k}_8\,|\,-\mathbf{k}_{13},\mathbf{k}_3\\ \mathbf{k}_{13}\,|\,-\mathbf{k}_3,-\mathbf{k}_8\end{pmatrix}+\begin{pmatrix}\mathbf{k}_4\,|\,\mathbf{k}_5,-\mathbf{k}_8\\ \mathbf{k}_5\,|\,-\mathbf{k}_8,\mathbf{k}_4\\ \mathbf{k}_8\,|\,-\mathbf{k}_4,-\mathbf{k}_5\end{pmatrix}$$

$$+\begin{pmatrix}\mathbf{k}_4\,|\,\mathbf{k}_6,-\mathbf{k}_9\\ \mathbf{k}_6\,|\,-\mathbf{k}_9,\mathbf{k}_4\\ \mathbf{k}_9\,|\,-\mathbf{k}_4,-\mathbf{k}_6\end{pmatrix}+\begin{pmatrix}\mathbf{k}_4\,|\,-\mathbf{k}_7,\mathbf{k}_{10}\\ \mathbf{k}_7\,|\,-\mathbf{k}_{10},-\mathbf{k}_4\\ \mathbf{k}_{10}\,|\,\mathbf{k}_4,-\mathbf{k}_7\end{pmatrix}+\begin{pmatrix}\mathbf{k}_4\,|\,\mathbf{k}_7,-\mathbf{k}_{13}\\ \mathbf{k}_7\,|\,-\mathbf{k}_{13},\mathbf{k}_4\\ \mathbf{k}_{13}\,|\,-\mathbf{k}_4,-\mathbf{k}_7\end{pmatrix}\Bigg\}. \tag{5}$$

The following remarks are in order: (i) the column vector

$$\mathbf{u}^{\mu}(\mathbf{k},t)=[u^{\mu}(\mathbf{k}_1),u^{\mu}(\mathbf{k}_2),\ldots,u^{\mu}(\mathbf{k}_{13})]$$

subsumes all flow variables of 13 wavevectors; (ii) the overhead dot denotes $\partial/\partial t$; (iii) the viscosity has been suppressed; (iv) each column vector of the right-hand side has 13 entries; shown explicitly in (5) are the non-zero entries, compressing out all zeros.

Since each column vector signifies a fundamental triad interaction, the intent of (5) is to show the 22 fundamental triad interactions coupled over 13 wavevectors at this level of truncation. Although (5) is meant to be schematic, it nevertheless conveys all the information necessary to generate the dynamic equation by the following rules. (i) Each entry of the column vector represents a term of the form

$$\sum_{\lambda,\rho}\overline{\phi}^{\mu|\lambda,\rho}_{\cdot|\cdot,\cdot}\,u^{\lambda *}(\cdot)\,u^{\rho *}(\cdot).$$

(ii) The dots are then supplied by the triad-wavevector entry. First, the triad wavevector as a whole represents the subscript of $\overline{\phi}$. Second, the arguments of $u^{\lambda *}(\cdot)$ and $u^{\rho *}(\cdot)$ are given by the two wavevectors in the order in which they appear after a vertical bar. For instance, the entries of the first column vector of (5) do indeed represent the first three non-zero entries, all others being zero. Then, by the aforementioned rules we can at once write down

$$\begin{pmatrix}\sum_{\lambda,\rho}\overline{\phi}^{\mu|\lambda,\rho}_{\mathbf{k}_1|\mathbf{k}_2,-\mathbf{k}_3}(\xi)\,u^{\lambda *}(\mathbf{k}_2)\,u^{\rho *}(-\mathbf{k}_3)\\ \sum_{\lambda,\rho}\overline{\phi}^{\mu|\lambda,\rho}_{\mathbf{k}_2|-\mathbf{k}_3,\mathbf{k}_1}(\xi)\,u^{\lambda *}(-\mathbf{k}_3)\,u^{\rho *}(\mathbf{k}_1)\\ \sum_{\lambda,\rho}\overline{\phi}^{\mu|\lambda,\rho}_{\mathbf{k}_3|-\mathbf{k}_1,-\mathbf{k}_2}(\xi)\,u^{\lambda *}(-\mathbf{k}_1)\,u^{\rho *}(-\mathbf{k}_2),\\ 0\\ \vdots\\ 0\end{pmatrix},$$

and the expression for the remaining column vectors may be recovered similarly.

When the wavevector lattice is larger than that of figure 1, it becomes all but impracticable to enumerate (3) by hand. However, there is no need to despair, because the

Upper k^2	Wavenumber radius	Wavevectors	Triad interactions or column vectors	Notation
3	1·73	13	22	$D(13)$
5	2·24	28	106	$D(28)$
7	2·56	40	242	$D(40)$
9	3	61	549	$D(61)$
11	3·32	85	1059	$D(85)$
16	4	128	2522	$D(128)$
25	5	257	10186	—
36	6	462	33152	—

TABLE 1. Some lower-order spherical truncations

enumeration can readily be carried out with the aid of a computer, thereby systematically sorting out the triad wavevectors allowed in a wavevector lattice of given truncation order. (From a computational standpoint, this enumeration once performed would eliminate the costly convolution summations.) It must be noticed that the 13 wavevectors of figure 1 all lie in a sphere of wavenumber radius $k = \sqrt{3}$, and no other wavevectors exist in that sphere. Hence (5) represents the spherical truncation of wavenumber radius $k = \sqrt{3}$. Summarized in table 1 are the pertinent results of spherical truncations up to the wavenumber radius $k = 6$.

As seen from table 1, the numbers of wavevectors and, particularly, of fundamental triad interactions increase very rapidly with the truncation order. Even for a relatively low order truncation of wavenumber radius $k = 6$, compared with Orszag & Patterson's (1972) simulation code of $k = 16$, the 462 wavevectors give rise to 924 (462×2) dynamic variables. Hence the corresponding system would have 924 complex differential equations with 33152 right-hand-side column vectors; a non-trivial numerical task. For future reference, the first six truncated systems of table 1 will be denoted by $D(N)$, where N is the number of wavevectors retained.

4. Theoretical background

Because of many degrees of freedom, the investigation of $D(N)$ will have to rely heavily on numerical analyses. It is therefore essential that a theoretical framework exists to guide us on what to compute and how to interpret it in support (or rejection) of certain dynamical propositions. To provide such theoretical guidance, it is necessary for us to review some basic results of classical statistical mechanics and modern dynamical systems, which are relevant to the present conservative (inviscid) system. To begin with, let us simplify the notation by writing $u_i^\mu(t) = u^\mu(\mathbf{k}_i, t)$. It is more advantageous to resolve the motion of $u_i^\mu(t)$ by the polar representation

$$u_i^\mu(t) = R_i^\mu(t) \exp\left(i2\pi\omega_i^\mu(t)\right)$$

into action $J_i^\mu = (R_i^\mu)^2$ and angle ω_i^μ. Because of the periodicity $\omega_i^\mu = [\omega_i^\mu, \mathrm{mod}\,(1)]$, the identical points in rectangular representation u_i^μ may have an angle difference of integer multiples.

4.1. *Energy and helicity conservations*

For a given $\mathbf{k}_i$, consider the Hermitian matrix

$$\begin{pmatrix} u_i^1 u_i^{1*} & i u_i^1 u_i^{2*} \\ -i u_i^2 u_i^{1*} & u_i^2 u_i^{2*} \end{pmatrix}. \tag{6}$$

It has been shown (Lee 1975) that the trace is modal energy $E_i = |u_i^1|^2 + |u_i^2|^2$ and the sum of the off-diagonals times k_i is modal helicity $H_i = ik_i(u_i^1 u_i^{2*} - u_i^2 u_i^{1*})$, ignoring any constant factor. The total energy and helicity are then

$$E = \sum_{i=1}^{N} \sum_{\mu=1,2} |u_1^\mu|^2 = \sum_{i=1}^{N} \sum_{\mu=1,2} J_i^\mu,$$

$$H = i \sum_{i=1}^{N} k_i (u_i^1 u_i^{2*} - u_i^2 u_i^{1*}) = 2 \sum_{i=1}^{N} k_i R_i^1 R_i^2 \sin 2\pi(\omega_i^1 - \omega_i^2),$$

in both representations.

Now, write the sum of all four elements of (6) in a Hermitian form $U_i^+ \mathscr{A} U_i$, where U_i is the column vector (u_i^1, u_i^2),

$$\mathscr{A} = \begin{pmatrix} 1 & i \\ -i & 1 \end{pmatrix},$$

and $+$ denotes the transjugate. Since the eigenvalues of $\mathscr{A}$ are 0 and 2, $U_i^+ \mathscr{A} U_i$ is positive semi-definite. Note that $U_i^+ \mathscr{A}^+ U_i$ is also positive semi-definite, for $\mathscr{A}$ and $\mathscr{A}^+$ have the same eigenvalues. Yet $U_i^+ \mathscr{A} U_i$ and $U_i^+ \mathscr{A}^+ U_i$ have different signs for their imaginary part; hence we infer from these quadratics that

$$|u_i^1|^2 + |u_i^2|^2 \geqslant |i(u_i^1 u_i^{2*} - u_i^2 u_i^{1*})|.$$

Or, in polar representation,

$$J_i^1 + J_i^2 \geqslant 2R_i^1 R_i^2 |\sin 2\pi(\omega_i^1 - \omega_i^2)|. \tag{7}$$

Multiplying both sides by k_i and summing over i, we have

$$\sum_{i=1}^{N} k_i E_i \geqslant |H|.$$

Its statistical form in isotropic field is $k\mathscr{E}(k) \geqslant |\mathscr{H}(k)|$, where $\mathscr{E}(k)$ and $\mathscr{H}(k)$ are respectively the isotropic energy and helicity spectra (Brissaud *et al.* 1973; Kraichnan 1973).

4.2. *Classical Liouville theorem*

By splitting u_i^μ into the real and imaginary parts, $u_i^\mu = v_i^\mu + iw_i^\mu$, we find from (3) the incompressibility of phase space

$$\sum_{i=1}^{N} \sum_{\mu=1,2} (\partial \dot{v}_i^\mu / \partial v_i^\mu + \partial \dot{w}_i^\mu / \partial w_i^\mu) = 0;$$

hence the volume element in phase space is an integral invariant. Or

$$\sum_{i=1}^{N} \sum_{\mu=1,2} (\partial \dot{J}_i^\mu / \partial J_i^\mu + \partial \dot{\omega}_i^\mu / \partial \omega_i^\mu) = 0$$

in action-angle variables (but not in R_i^μ and ω_i^μ, for they are not canonical variables). This is the content of the classical Liouville theorem, stating the preservation of

measure under the time evolution. Clearly the Liouville theorem will not hold in the presence of viscous damping; hence, it is a property of inviscid flow (conservative) systems. It was almost 30 years ago that T. D. Lee (1952) first showed that the Navier–Stokes equations in Fourier space obey the classical Liouville theorem. Although the measure-invariance is necessary for ergodicity and mixing (defined in § 4.3), it is too presumptuous to infer ergodicity and, particularly, energy equipartition from the Liouville theorem alone (as is often implied in the literature).

There are several technical comments. First, dynamical systems with an invariant measure return arbitrarily close to the initial points (recurrence theorem, Nemytskii & Stepanov 1960, chap. 6). However, the recurrence time (frequency of return), which is not given by the theorem, may be extremely long for a large-degree-of-freedom system (Hemmer 1959). Hence the return to initial state is practically inconceivable for $D(N)$ even under the assumption of no chaos. Secondly, all recurrence motions are central motions, but the converse is not true (Birkhoff 1927, p. 198). Lastly, because of the measure invariance, the trajectory of an inviscid flow will not wind down to a submanifold of phase space. Hence one does not usually speak of an attractor of conservative systems, although an attractor may be defined to encompass the whole state space (Lanford 1976).

4.3. *Ergodicity and mixing*

For each $\mathbf{k}_i$ there are two components $u_i^\mu(t)$ for $\mu = 1$ and 2, each of which in turn splits into either v_i^μ and w_i^μ or R_i^μ and ω_i^μ. We can therefore span the phase space of $D(N)$ by the co-ordinates $\mathbf{x} = \{x_1, x_2, \ldots, x_{4N}\}$ in $4N$-dimensional Euclidean space. First of all, the trajectory of $D(N)$ must lie on the surface of constant energy and helicity (§ 4.1). Because of the measure invariance (§ 4.2), the initial volume element of, say, a unit $(4N-2)$-dimensional sphere will spread over the constant energy–helicity surface, but without suffering any volume change. Ergodicity and mixing are the criteria on the shape of spreading volume element and the manner in which it proceeds. For phase function $f(\mathbf{x})$ along a trajectory, one can compute the time average over a period t by $\bar{f}(\mathbf{x}, t) = t^{-1}\int_0^t f(\mathbf{x}, s)\, ds$. According to Birkhoff's theorem (Khinchin 1949, p. 19), this average over a sufficiently long time, i.e. $\lim_{t\to\infty} \bar{f}(\mathbf{x}, t)$, approaches a constant value $\bar{f}(\mathbf{x})$ for almost all initial conditions, when the trajectory is restricted to the invariant part of phase space. After the trajectory has traversed every extension of the phase space with equal frequencies, it is reasonable to expect that $\bar{f}(\mathbf{x})$ should be close to that obtained by averaging $f(\mathbf{x})$ over all possible extensions of the phase space. We shall denote the phase average symbolically by $\langle f(\mathbf{x})\rangle = \int_S f(\mathbf{x})\, d\mu(S)$, where $\mu(S)$ is a normalized measure of the constant energy–helicity surface S. The system is said to be ergodic if and only if

$$\lim_{t\to\infty} \bar{f}(\mathbf{x}, t) = \langle f(\mathbf{x})\rangle. \tag{8}$$

Clearly, if the trajectory is restricted to part of the phase space or if the phase space is split into two invariant parts of non-zero measure (metric decomposability), then it is not possible to guarantee ergodicity. Hence the condition of metric in-decomposability has long been used synonymously with ergodicity.

The numerical testing of ergodicity runs into two difficulties. First, the equality (8) should be checked out for all phase functions. Should there be found a phase function violating (8), the ergodic claim is nullified. In practice, however, ergodicity is under-

stood to have been claimed for a certain class of measurable phase functions of physical importance (see Kells & Orszag (1978) and Glaz (1981) for the choice of phase functions for two-dimensional turbulence). The second difficulty is that the ergodic theorem is a statement about the equilibrium trajectory in the limit as $t \to \infty$. One may then ask why we cannot evolve $D(N)$ over a sufficiently long time to test (8) in a sort of numerical quasi-equilibrium sense. Unfortunately, the answer is negative because of the emergence of a random or chaotic trajectory. Consequently, numerical trajectory evolution is restricted to several characteristic correlation times of a typical dynamic variable. Complete chaos is referred to as mixing in the phase space, which has the everyday analogy of mixing cream into a cup of coffee. Quantitatively, for any measurable functions $f(\mathbf{x})$ and $g(\mathbf{x})$ the system is said to be (strong) mixing if (Arnold & Avez 1968, theorem 9.8)

$$\lim_{t\to\infty} \langle f(\mathbf{x},t)\, g(\mathbf{x})\rangle = \langle f(\mathbf{x})\rangle \langle g(\mathbf{x})\rangle. \tag{9}$$

Intuitively, in an ergodic system the trajectory covers every extension of the phase space with equal frequencies. However, when it does so in a random fashion the system is mixing. Mixing, therefore, implies ergodicity, but not *vice versa*.

4.4. *Ergodic definition of Khinchin*

As pointed out in § 4.3, ergodicity and metric indecomposability have long been defined in terms of each other. Khinchin has therefore attempted to define ergodicity without resorting to the metric indecomposability. Let us begin by assuming that

$$\langle f(\mathbf{x})\rangle = 0. \tag{10}$$

This zero-mean condition is subject to verification, although it is plausible for $f(\mathbf{x})$, which is a function of a single Fourier mode. Define a correlation function with respect to the zero initial time:

$$\rho(t) = \langle f(\mathbf{x},t) f(\mathbf{x},0)\rangle / \langle f^2(\mathbf{x})\rangle.$$

Then Khinchin's theorem states that if $\rho(t) \to 0$ for $t \to \infty$ the function $f(\mathbf{x})$ is ergodic (Khinchin 1949, p. 68). In fact, the claim of this theorem is too modest; it further implies mixing. To see this, we write (9) for $f = g$:

$$\lim_{t\to\infty} \langle f(\mathbf{x},t) f(\mathbf{x},0)\rangle = \langle f(\mathbf{x})\rangle \langle f(\mathbf{x})\rangle = 0. \tag{11}$$

The second equality follows from (10). (The derivation of (11) is also found in Lebowitz (1972).) Since (11) is precisely the ergodic condition of Khinchin, his theorem may be considered more correctly as a mixing than an ergodic theorem.

Since ergodicity does not imply mixing, one would never test for mixing unless $f(\mathbf{x})$ is known or suspected to be ergodic. In other words, the establishment of ergodicity precedes the test for mixing. Since ergodicity means that phase and time averages are the same, we may recast $\rho(t)$ into the autocorrelation of the phase function evolved over T,

$$\rho(T,\tau) = \int_0^{T-\tau} f(\mathbf{x}, s+\tau) f(\mathbf{x}, s)\, ds \Big/ \int_0^{T-\tau} f^2(\mathbf{x}, s)\, ds, \tag{12}$$

defined similarly to that of Kells & Orszag (1978) for two-dimensional turbulence. Whence the content of Khinchin's theorem is

$$\lim_{\tau\to\infty} \rho(T,\tau) = 0$$

for $T > \tau$ sufficiently large for good data sampling.

4.5. *Microcanonical distribution*

We shall now express the normalized measure $\mu(S)$ of § 4.3 in terms of the phase-space co-ordinates. To this end, we write the modal energy and helicity in the Hermitian quadratic form

$$E_i = U_i^\dagger \mathscr{I} U_i, \quad H_i = U_i^\dagger \mathscr{B}_i U_i,$$

where $\mathscr{I}$ is the unit matrix and

$$\mathscr{B}_i = \begin{pmatrix} 0 & -ik_i \\ ik_i & 0 \end{pmatrix}.$$

By the transformation

$$\mathscr{U}_i = 2^{-\frac{1}{2}} \begin{pmatrix} 1 & i \\ i & 1 \end{pmatrix} Y_i,$$

the E_i and H_i become diagonal (though E_i already is) in $Y_i = (y_i^1, y_i^2)$. Extending the similarity transformation to the sums of E_i and H_i, we find that

$$E = \sum_{i=1}^{N} |y_i^1|^2 + |y_i^2|^2, \quad H = \sum_{i=1}^{N} k_i(|y_i^1|^2 - |y_i^2|^2).$$

Now, rearranging the real and imaginary parts of y_i in a sequence of $4N$ variables, and identifying this sequence with the $\mathbf{x}$-co-ordinates already introduced in § 4.3, the total energy and helicity may be put in the real quadratic form

$$E(\mathbf{x}) = \sum_{i=1}^{4N} x_i^2, \quad H(\mathbf{x}) = \sum_{i=1}^{4N} c_i x_i^2.$$

Here c_i are not all distinct, and exactly half of them are negative.

Since the energy–helicity surface is of the same type of quadratic constraint as the energy–enstrophy surface, by parroting the result of two-dimensional turbulence (Glaz 1977, Lee 1982) we can at once extend the classical Khinchin theorem to three-dimensional turbulence:

$$\frac{\partial^2}{\partial E\, \partial H} \int_V f(\mathbf{x})\, d\mathbf{x} = \int_S f(\mathbf{x}) \frac{d\Sigma}{|\operatorname{grad} E|\, |\operatorname{grad} H| \sin\theta}. \tag{13}$$

Here θ is the angle between grad E and grad H, and $d\Sigma$ is a differential element of S. The parametrization of $d\Sigma$ in terms of $4N-2$ co-ordinates may follow the procedure of two-dimensional turbulence. To complete the discussion of the right-hand side, however, it is necessary to show that S is smooth and connected (as was done by Glaz (1977) for the energy–enstrophy surface), which will not be pursued here. For the left-hand side V is the intersection of two phase spaces enclosed respectively by the constant energy and helicity surfaces. By extending the $\mathbf{x}$-integration over all phase space with the use of unit step functions, an alternative form of (13) is obtained:

$$\int f(\mathbf{x})\, \delta(E - E(\mathbf{x}))\, \delta(H - H(\mathbf{x}))\, d\mathbf{x} = \int_S f(\mathbf{x}) \frac{d\Sigma}{|\operatorname{grad} E|\, |\operatorname{grad} H| \sin\theta}.$$

We have thus established equivalence of the microcanonical distributions

$$\delta(E - E(\mathbf{x}))\, \delta(H - H(\mathbf{x}))$$

over all of $\mathbf{x}$-space and $1/|\operatorname{grad} E|\, |\operatorname{grad} H| \sin\theta$ on the energy–helicity surface S.

For instance, in terms of the latter distribution, the normalized measure $\mu(S)$ gives rise to

$$d\mu(S) = \frac{d\Sigma}{\Omega(S)\,|\mathrm{grad}\,E|\,|\mathrm{grad}\,H|\sin\theta},$$

where $\Omega(S) = \int_S d\Sigma/|\mathrm{grad}\,E|\,|\mathrm{grad}\,H|\sin\theta$ is the so-called structural function (Khinchin 1949, p. 37).

4.6. *Canonical distribution*

Logically speaking, the canonical distribution is the asymptotic form of the *a priori* probability density $d\Sigma/|\mathrm{grad}\,E|\,|\mathrm{grad}\,H|\sin\theta$ on the energy–helicity surface in the limit as $N \to \infty$. The Gaussian distribution then emerges as a consequence of the central-limit theorem (Khinchin 1949, chap. 5). More provincially, however, we can write down the Gaussian canonical distribution as a function of the sum of constants of motion $C_1 E_i + C_2 H_i$, where C_1 and C_2 are constants (Lee 1975):

$$\prod_{i=1}^{N} \frac{(C_1^2 - C_2^2 k_i^2)^{\frac{1}{2}}}{\pi^2} \exp\{-C_1(|u_i^1|^2 + |u_i^2|^2) - iC_2 k_i (u_i^1 u_i^{2*} - u_i^2 u_i^{1*})\}.$$

In fact, this is an equilibrium solution of the Liouville equation and, moreover, is a stable equilibrium distribution (Kraichnan 1973). We first note the difference between the microcanonical and canonical distributions: the former is an *a priori* distribution on the constant energy–helicity surface S, whereas the latter is a Gaussian distribution extending over all phase space. How can they then be related? To see this, recall the alternative expression of the microcanonical distribution, $\delta(E - E(\mathbf{x}))\,\delta(H - H(\mathbf{x}))$, which is peaked infinitely sharply on the submanifold S. Although a Gaussian distribution cannot peak out as sharply as the Dirac delta function, when we consider only a single component of u_i^μ the canonical distribution becomes more pronouncedly peaked about S as there are more components of u_i^μ included in the exponent. This is how the canonical (Gaussian) distribution can approximate the microcanonical (delta-function) distribution closely as N becomes large.

Averaging over the canonical distribution, we find that (Lee 1975)

$$\langle |u_i^1|^2 \rangle = \langle |u_i^2|^2 \rangle = \frac{C_1}{C_1^2 - C_2^2 k_i^2}, \tag{14a}$$

$$\langle u_i^2 u_i^{1*} \rangle = -\langle u_i^1 u_i^{2*} \rangle = \frac{iC_2 k_i}{C_1^2 - C_2^2 k_i^2}. \tag{14b}$$

Let us examine the consequence of (14). First, when helicity is zero $C_2 = 0$, hence energy equipartition follows:

$$\langle |u_i^1|^2 \rangle = \langle |u_i^2|^2 \rangle = 1/C_1 \quad \text{for all } i. \tag{15}$$

Secondly, in general $C_2 \neq 0$ for non-zero helicity. Then (14*a*) implies the equality of modal energy distributions for u_i^1 and u_i^2, although there is no equipartition among i. Thirdly, (14*b*) gives the equilibrium helicity distribution $2C_2 k_i^2/(C_1^2 - C_2^2 k_i^2)$. Lastly, since $\langle u_i^1 u_i^{2*} \rangle$ and $\langle u_i^2 u_i^{1*} \rangle$ are purely imaginary, (14*b*) implies the vanishing of the real part of the reflectional asymmetry, which is a condition for isotropy to be discussed in § 4.7.

4.7. *Isotropy of the covariance spectral tensor*

In three-dimensional turbulence, the isotropy requirements for the covariance spectral tensor are the spherical, rotational and reflectional symmetries (Lee 1979). In inviscid flow, both the spherical and rotational symmetries are realized by the energy equipartition. The reflectional asymmetry, however, manifests itself in real and imaginary parts. Helicity is the imaginary part of the reflectional asymmetry, which we can at will set equal to zero since it is a constant of motion. Hence the real part of the reflectional asymmetry given by

$$U_4 = \sum_{i=1}^{N} (u_i^1 u_i^{2*} - u_i^2 u_i^{1*}) = 2 \sum_{i=1}^{\infty} R_i^1 R_i^2 \cos 2\pi(\omega_i^1 - \omega_i^2) \tag{16}$$

is the only thing that remains to be examined. According to (14*b*), the phase-average $\langle U_4 \rangle$ vanishes identically. Hence isotropy of the covariance spectral tensor is indeed consistent with the canonical distribution.

4.8. *Kolmogorov entropy*

Mixing is engendered by the trajectory instability, whereby the two nearby trajectories become separated exponentially in phase space with the evolution time; hence it is also called the exponential orbit separation (Sinai 1973). Consider an open set of initial states. If the system is mixing, the initial open set will spread out randomly (e.g. Lee 1979, figure 10) and eventually cover the entire energy–helicity surface in the limit as $t \to \infty$. In fact, the open set of trajectories does not grow in actual size owing to measure invariance. It is the mutual distance of trajectories that becomes large as evolution proceeds. Trajectory instability can be quantified by the Kolmogorov entropy adapted from the one proposed by Benettin, Galgani & Strelcyn (1976). To define such a metric entropy, however, calls for explicit computation of trajectories of initial proximity. Since the trajectory is dependent on the initial condition I, the parameter ξ, and the initial T_0 and final evolution time T, we shall adopt the notation $D(N, I, \xi, T_0, T)$ to include all the parameters. (Note that $D(N)$ is still reserved for a generic notation when the parameter values are of no direct concern.)

Let us denote by U the trajectory of $D(N, I, \xi, T_0, T)$ on the constant energy–helicity surface. As mentioned in § 4.2, the representation of U may consist of the real and imaginary components v_i^μ and w_i^μ, respectively. To speak precisely of the distance of another trajectory U' with the corresponding components $v_i'^\mu$ and $w_i'^\mu$, from U we introduce a Euclidean norm

$$\| U - U' \| = \left[\sum_{i=1}^{N} \sum_{\mu=1,2} (v_i^\mu - v_i'^\mu)^2 + (w_i^\mu - w_i'^\mu)^2 \right]^{\frac{1}{2}}. \tag{17}$$

At $T_0 = 0$ we consider an initial condition I_0 that is removed from I by a small distance d, i.e. $\| I - I_0 \| = d$, and evolve the trajectory from it over a pre-assigned time interval $\Delta\tau$. At the end of the first time interval $(0, \Delta\tau)$, we then compute the trajectory distance by

$$d_1 = \| D(N, I, \xi, 0, \Delta\tau) - D(N, I_0, \xi, 0, \Delta\tau) \|.$$

Note that the trajectories of $D(N, I, \xi, 0, \Delta\tau)$ and $D(N, I_0, \xi, 0, \Delta\tau)$ do not necessarily lie on the same energy–helicity surface. Now, for the second time interval $(\Delta\tau, 2\Delta\tau)$, we specify a new initial point I_1 that is again a distance d away from the U at $T = \Delta\tau$,

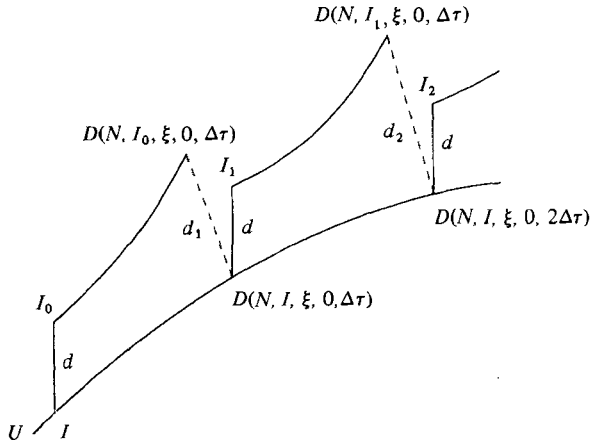

FIGURE 2. Computational schematics for Kolmogorov entropy.

i.e. $D(N, I, \xi, 0, \Delta\tau)$. After evolving the trajectory from I_1 over $\Delta\tau$, we compute the trajectory separation by

$$d_2 = \|D(N, I, \xi, 0, 2\Delta\tau) - D(N, I_1, \xi, 0, \Delta\tau)\|,$$

for the second time interval $(\Delta\tau, 2\Delta\tau)$. In a similar fashion, the trajectory separation of successive time intervals can be computed to yield a sequence of positive numbers $\{d_j\}$ for $j = 1, 2, 3, \ldots$. Figure 2 schematizes the computation of $\{d_j\}$, which differs from figure 1 of Benettin *et al.* (1976) in that, for instance, I_1 is not in general required to lie on the dotted-line segment connecting $D(N, I, \xi, 0, \Delta\tau)$ and $D(N, I_0, \xi, 0, \Delta\tau)$. As will be discussed in § 6, however, this difference is irrelevant. Benettin *et al.* (1976) defined an entropy-like quantity by

$$k_n(\Delta\tau, U, d) = \frac{1}{n\Delta\tau} \sum_{j=1}^{n} \ln (d_j/d).$$

They have observed from the numerical study of a Hamiltonian system (e.g. the Hénon–Heiles (1964) model) that when U is in regions of the phase space exhibiting chaos then (i) the long-time limit of summation settles down to a constant value, i.e. $\lim_{n\to\infty} k_n(\Delta\tau, U, d) = k(\Delta\tau, U, d)$ for suitably chosen $\Delta\tau$ and d, (ii) $k(\Delta\tau, U, d)$ is independent of $\Delta\tau$, and (iii) $k(\Delta\tau, U, d)$ is independent of d. Under these conditions we may identify $k(\Delta\tau, U, d)$ with the Kolmogorov entropy (Lyapunov characteristic numbers). A dynamical system with positive Kolmogorov entropy is called a 'K-system', which is a stronger characterization than mixing (Sinai 1973).

For non-random trajectories (including a quasi-periodic motion), on the other hand, $\lim_{n\to\infty} k_n(\Delta\tau, U, d)$ is non-positive. Hence the Kolmogorov entropy can provide a means for discerning stochastic islands of the phase space from the ordered (non-random) region.

4.9. *Trajectory instability*

Trajectory instability, to be distinguished from numerical instability, has been encountered for a long time in fluid dynamics, although it has only recently been identified as such. The first evidence was reported more than 20 years ago by Birkhoff & Fisher (1959), who observed irregular evolution of the initially smooth vortex sheets modelled

by discrete point vortices. Their work, however, did not receive due attention because the idea of an irregular fluid trajectory was incompatible with computational fluid dynamics. Nevertheless, trajectory instability has resurfaced in the late 1960s, but now in the numerical prediction of meteorological flows (Robinson 1967, Lorenz 1969). It is the so-called predictability or error-growth problem in numerical weather forecasting, the viability of which is known to be limited to only a few days (Leith 1978). However, considerable evidence accumulated in recent years clearly indicates that trajectory instability manifested by the limited evolution time is not an isolated incident. In fact, it occurs in a variety of model flow problems, such as the Bénard convection problem (McLaughlin 1976), the inviscid Burger's model (Lee 1980) and two-dimensional inviscid turbulence (Glaz 1981).

As a matter of fact, trajectory instability manifests itself in a dichotomic manner. On the one hand, it gives rise to the sensitive dependence of $D(N)$ on the initial condition. Since this implies the loss of initial information, $D(N)$ can exhibit macroscopic irreversibility of a trajectory motion that is dynamically reversible; an ingredient necessary for statistical mechanics. It must be pointed out that Ruelle (1979) has recently proposed the asymptotic decay of the time-correlation function defined exactly as in (11) as a practical test for the sensitive dependence of dynamical systems on the initial condition.

On the other hand, one cannot compute the trajectory over a long time period because of the accumulation of round-off errors. Note that digital computers have a finite accuracy, and numerical trajectory computation is, at best, an attempt to approximate the true orbit (integral curve) with a finite number of digits. At any time step of integration, therefore, the difference in numerical and true orbits, however small it may be, will grow exponentially by the very definition of trajectory instability. The computed orbit will eventually depart from the true trajectory drastically; hence it is called a pseudo-orbit.

For the Anosov system (Y-system), however, the dichotomy of trajectory instability can be conciliated, and can thereby provide a logical link between dynamics and statistics. Benettin *et al.* (1978) have shown that for Anosov systems time averages computed from a pseudo-orbit are identical with those computed from the true orbit, although the pseudo-orbit may be completely different from the true orbit. This is based on a theorem of Anosov and Bowen which states roughly that near a pseudo-orbit of an Anosov system there are (infinitely) many true trajectories (originating, of course, from some other initial states), all of which would give rise to the same time average over a long time. Intuitively speaking, since the Anosov system is a model of a completely unstable system, one may expect that the deviation of the pseudo-orbit from the true orbit is so random that its time-averaged effect is zero owing to cancellations.

Since the claim of Benettin *et al.* (1978) has also been verified on stochastic systems which are not strictly of Anosov's type, we shall assume that their work is applicable to our system $D(N)$. This then enables us to compute time averages much beyond the evolution time for the true trajectory.

Summing up, trajectory instability presents us with a choice: either to formulate the turbulence problem for long-time statistics, or to simulate it numerically but only for a short-time dynamics. We therefore come to echo Prigogine's (1979) view that statistics begins where dynamics stops.

5. Effective evolution time of the lowest-order system

In this paper, the numerical integration was performed by the solver package ODE developed and documented by Shampine & Gordon (1975). At the risk of misquoting, let us venture to say that the ODE is a variable-step, variable-order Adams–Bashford predictor and Adams–Moulton corrector code. Since the internal working of ODE is of no direct concern, we shall restrict ourselves here to the use of it as a black box, but communicating only with the input/return flag (IFLAG). Both the relative and absolute error tolerances, RELERR and ABSERR, are used to control the local error by

$$|\text{local error}| = \text{RELERR}^*|\text{approximated } u_i^\mu| + \text{ABSERR}.$$

Since by design $u_i^\mu \leqslant 1$, we shall always set RELERR = 0 and specify only the absolute error tolerance. By successively reducing ABSERR by the factor of 0·1, i.e. ABSERR = 10^{-7}, 10^{-8}, etc. it was found that on CDC CYBER 74/175 the smallest ABSERR that ODE can cope with is 10^{-13}. (In other words, ODE will automatically boost the error tolerance when ABSERR = 10^{-14} is imposed.) That this is perhaps the smallest ABSERR may be seen from the unit round-off error of CDC single precision, which Shampine & Gordon (1975) have estimated to be $7{\cdot}1 \times 10^{-15}$. Hence, all numerical experiments were carried out with RELERR = 0 and ABSERR = 10^{-3}, unless otherwise stated.

Shampine & Gordon (1975, p. 122) proposed a global error estimate by the reintegration, whereby one reintegrates the problem with the reduced error tolerance by an order of magnitude and compares the results (also adopted by Glaz (1977) for two-dimensional turbulence). However, this is not really relevant to our application of the open-ended evolution time. Rather, the pertinent question is how long can we evolve $D(N)$ before the accuracy of trajectory computation is in doubt. This question can best be dealt with by the forward–backward time integration, whereby one integrates the problem in forward time up to a predetermined value and then in backward time to recover the initial condition. (Note that ODE is well suited for this; one simply has to reverse the sign of the time step, $DT = -DT$, for the backward time integration.) When there is no accumulation of round-off errors, one should recover the initial data, of course, within the order of ABSERR, independent of the integration time period. Therefore, the recovery of initial data after a forward–backward time integration can provide an overall measure of computational accuracy.

For the test of initial data recovery, $D(13)$ was integrated in forward and backward times under the initial condition I_{13} defined by

$$I_n = \{R_i^\mu = (2n)^{-\frac{1}{2}},\ \omega_i^\mu = \tfrac{1}{8}\ (\mu = 1, 2;\ i = 1, 2, \ldots, n)\}.$$

The interpretation of I_n will be given in § 6. The forward–backward time integration was carried out for three $T = 110$, 120 and 130, but all under $\xi = \frac{3}{8}$ and ABSERR = 10^{-13}. The result of forward time evolution $D(13, I_{13}, \frac{3}{8}, 0, T)$ followed by backward time evolution $D(13, D(13, I_{13}, \frac{3}{8}, 0, T), \frac{3}{8}, T, 0)$ can best be summarized by superimposing the recovered initial data on the imposed initial data. Since I_{13} has equal action and angle for all modes, it is simply represented by a single point, denoted by $*$ in figure 3, in the phase plot of $\mathscr{R}(u_k^\mu)$ and $\mathscr{I}(u_k^\mu)$. For $T = 110$ the recovery of initial data appears quite good; at least as shown graphically in figure 3(*a*); the recovered initial data points, denoted by ○, coincide with the imposed initial-data

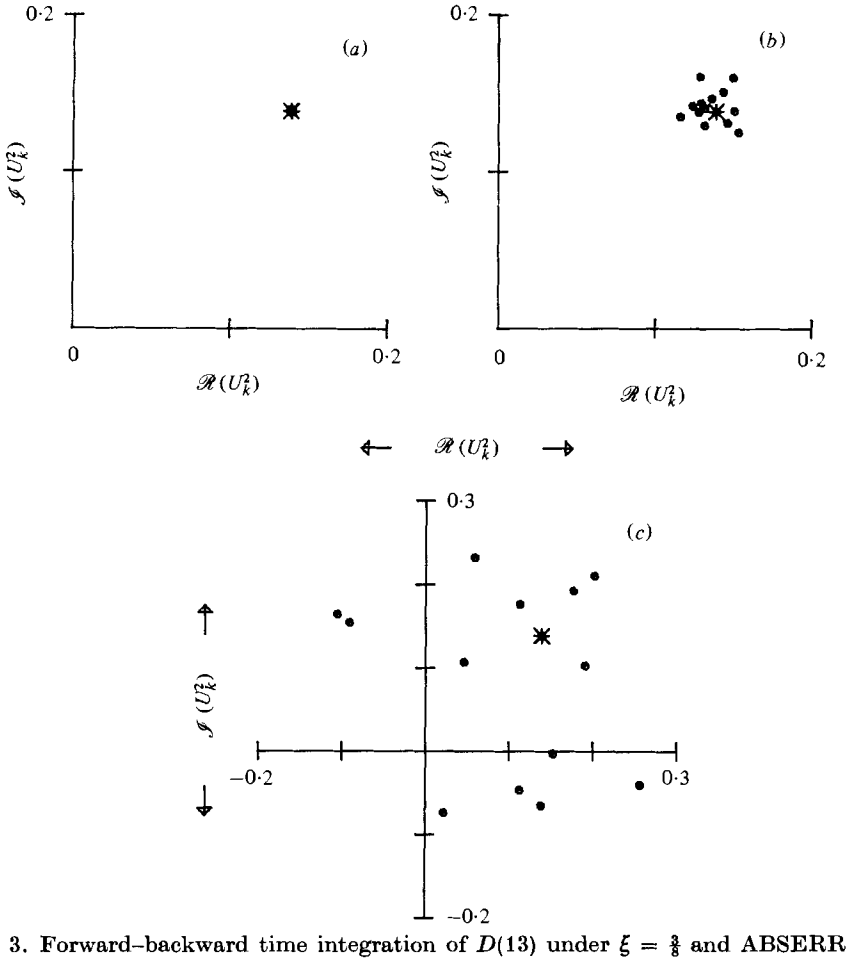

FIGURE 3. Forward–backward time integration of $D(13)$ under $\xi = \frac{3}{8}$ and ABSERR = 10^{-13}. ✳, initial condition I_{13}; ○, recovered initial data. (*a*) Evolution time $T = 110$; (*b*) $T = 120$; (*c*) $T = 130$.

point. Quantitatively, however, the deviations of recovered R_i^μ and ω_i^μ from the respective initial values $\sqrt{\frac{1}{26}}$ and $\frac{1}{8}$ do not exceed $\pm 0{\cdot}75\,\%$; hence this maximum deviation will hereinafter be adopted as a criterion of good recovery. With a slightly increased $T = 120$, figure 3(*b*) shows some scatter in the recovered initial data. But a further increase in T renders the recovery of initial data all but impossible; as attested to by the widely scattered data points of figure 3(*c*). Because of the periodicity $\omega_i^\mu = [\omega_i^\mu, \mathrm{mod}\,(1)]$ mentioned in § 4, figure 3(*c*) gives only a partial account of recovery failure in that the recovered initial data points may not all lie on the same Riemann sheet. To examine this, we have presented the time histories of ω_3^1 and ω_4^2 during the forward time integration in figure 4(*a*), and during the backward time integration in figure 4(*b*). Since the recovered ω_4^2 falls below the initial value $\frac{1}{8}$ by more than unity, we now know that the recovered u_4^2 of figure 3(*c*) lies in a Riemann sheet different from that of I_{13}.

In conclusion, based on the $\pm 0{\cdot}75\,\%$ maximum deviation, the largest T has been found to be 110 under ABSERR = 10^{-13}. Although T varies with the choice of I and ξ,

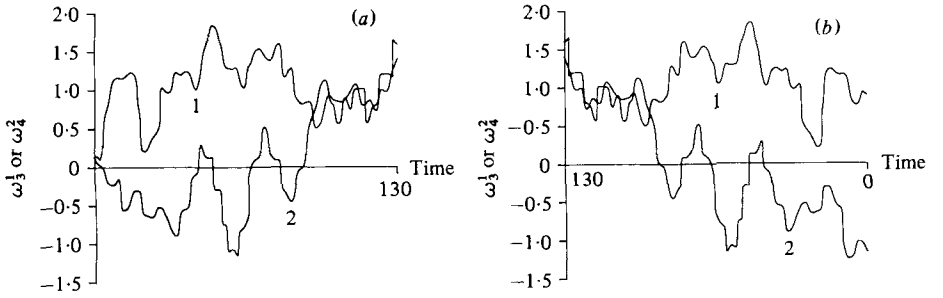

FIGURE 4. Time histories of ω_3^1 and ω_4^2. '1' = ω_3^1; '2' = ω_4^2. (*a*) Forward time integration $D(13, I_{13}, \frac{3}{8}, 0, 130)$. (*b*) Backward time integration $D(13, D(13, I_{13}, \frac{3}{8}, 0, 130), \frac{3}{8}, 130, 0)$.

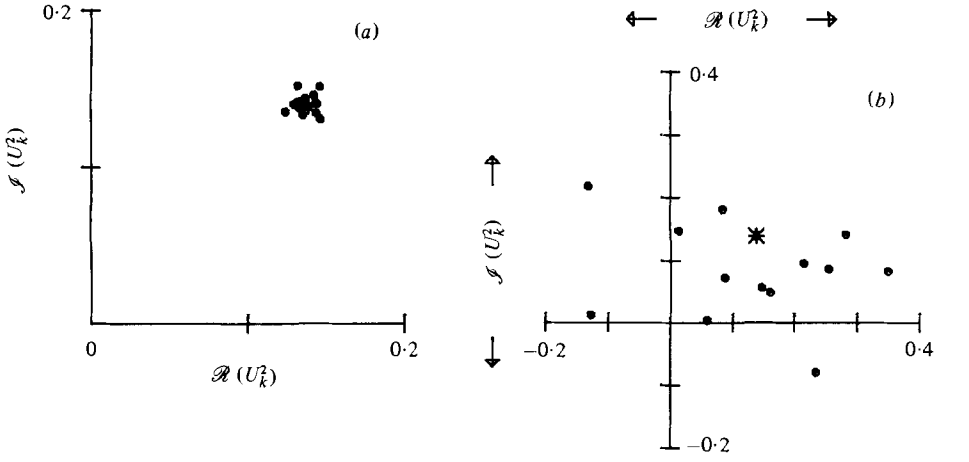

FIGURE 5. Forward–backward time integration of $D(13)$ under $\xi = \frac{3}{8}$ over the evolution time $T = 110$. ✳, initial condition I_{13}; ○, recovered initial data. (*a*) Error tolerance ABSERR = 10^{-12}; (*b*) ABSERR = 10^{-11}.

$\log_{10}$ (ABSERR)	Total number of derivative evaluations for $D(13, I_{13}, \frac{3}{8}, 0, 110)$	Reference
−13	8559	Figure 3(*a*)
−12	5429	Figure 5(*a*)
−11	3457	Figure 5(*b*)

TABLE 2. Comparison of the number of derivative evaluations

we shall take this T as a typical effective evolution time of $D(13)$, beyond which evolution would give a pseudo-orbit (§4.9). Now, to show strong dependence on the error tolerance, the forward–backward time integration of figure 3(*a*) has been repeated, but under less stringent error controls. Under ABSERR = 10^{-12} the recovered initial data of figure 5(*a*) show modest spread about I_{13}, whereas figure 5(*b*) clearly indicates that $T = 110$ is too large when the error tolerance is ABSERR = 10^{-11}.

Numerically, energy and helicity are conserved only approximately. We have observed that deviations in energy and helicity conservations are less than ABSERR by at least one order of magnitude within the effective evolution time. This is why

monitoring the energy and helicity conservations cannot forewarn of numerical catastrophe; a similar view was expressed by Glaz (1977) for the two-dimensional turbulence.

Departing for now from the numerical accuracy, the set of computations underlying figures 3(*a*), 5(*a*, *b*) can provide a comparison of computing costs, which escalate rapidly with the more stringent error tolerance. We have summarized in table 2 the total number of derivative evaluations incurred during the evolution of $D(13, I_{13}, \frac{3}{8}, 0, 110)$ under three ABSERRs.

Assuming that computing cost is directly proportional to the number of derivative evaluations, this being the case for a large system such as $D(13)$, one can infer from the table that tightening ABSERR by two orders of magnitude has resulted in more than doubling the computing cost.

6. Numerical results of the lowest-order system

Owing to the limited evolution time, it is not possible to provide a direct test for ergodicity (8) and mixing (9), which necessitates an equilibrium trajectory. According to the theoretical discussion of § 4, however, the limited evolution time is a sufficient numerical testimony of trajectory instability that is also possessed by K-systems and Anosov systems. We shall present here some numerical details of $D(13)$ that indicate ergodicity and mixing and isotropy of the covariance spectral tensor. As a matter of fact, we have shown something stronger; the $D(13)$ has a positive Kolmogorov entropy, and hence is a K-system.

By the polar transformation, the dynamic equation (5) can be expressed in terms of R_i^μ and ω_i^μ:

$$\begin{pmatrix} \dot{R}_1^\mu \\ \dot{R}_2^\mu \\ \dot{R}_3^\mu \\ . \\ . \\ . \end{pmatrix} = \sum_{\lambda,\rho} \left\{ \begin{pmatrix} -\overline{\phi}^{\mu|\lambda,\rho}_{\mathbf{k}_1|\mathbf{k}_2,-\mathbf{k}_3} R_2^\lambda R_3^\rho \sin 2\pi(\omega_1^\mu + \omega_2^\lambda - \omega_3^\rho) \\ -\overline{\phi}^{\mu|\lambda,\rho}_{\mathbf{k}_2|-\mathbf{k}_3,\mathbf{k}_1} R_3^\lambda R_1^\rho \sin 2\pi(\omega_1^\rho + \omega_2^\mu - \omega_3^\lambda) \\ -\overline{\phi}^{\mu|\lambda,\rho}_{-\mathbf{k}_3|\mathbf{k}_1,\mathbf{k}_2} R_1^\lambda R_2^\rho \sin 2\pi(\omega_1^\lambda + \omega_2^\rho - \omega_3^\mu) \\ 0 \\ 0 \\ 0 \end{pmatrix} + \ldots \right\}, \tag{18a}$$

$$\begin{pmatrix} \dot{\omega}_1^\mu \\ \dot{\omega}_2^\mu \\ \dot{\omega}_3^\mu \\ . \\ . \\ . \end{pmatrix} = \sum_{\lambda,\rho} \left\{ \begin{pmatrix} -(2\pi R_1^\mu)^{-1} \overline{\phi}^{\mu|\lambda,\rho}_{\mathbf{k}_1|\mathbf{k}_2,-\mathbf{k}_3} R_2^\lambda R_3^\rho \cos 2\pi(\omega_1^\mu + \omega_2^\lambda - \omega_3^\rho) \\ -(2\pi R_2^\mu)^{-1} \overline{\phi}^{\mu|\lambda,\rho}_{\mathbf{k}_2|-\mathbf{k}_3,\mathbf{k}_1} R_3^\lambda R_1^\rho \cos 2\pi(\omega_1^\rho + \omega_2^\mu - \omega_3^\lambda) \\ (2\pi R_3^\mu)^{-1} \overline{\phi}^{\mu|\lambda,\rho}_{-\mathbf{k}_3|\mathbf{k}_1,\mathbf{k}_2} R_1^\lambda R_2^\rho \cos 2\pi(\omega_1^\lambda + \omega_2^\rho - \omega_3^\mu) \\ 0 \\ 0 \\ 0 \end{pmatrix} + \ldots \right\}. \tag{18b}$$

Only the terms corresponding to the first right-hand-side column vector of (5) are shown here explicitly; the three dots represent the remaining 21 terms, readily expressible in a similar manner.

Numerically we shall always integrate the rectangular form rather than the polar (18). This is because the factors $(R_i^\mu)^{-1}$ that appear in the right-hand side of (18*b*) become unbounded at some time, so that the ω_i^μ equations will violate the Lipschitz condition there. Hence the consequence is the loss of uniqueness (Bellman 1953, p.

69), which is to be expected from the periodicity of polar representation as pointed out in § 4. The result of rectangular representation can then be expressed in action-angle variables in a straightforward manner. First, J_i^μ is the squared magnitude $|u_i^\mu|^2$. Secondly, ω_i^μ is computed by the convention that the positive (negative) angle is referred to the clockwise (counterclockwise) rotation.

From (18) we can at once infer the invariant set

$$\mathscr{S} = \{\text{arbitrary } R_i^\mu \text{ and } \omega_i^\mu \text{ such that } \omega_1^\mu + \omega_2^\lambda - \omega_3^\rho, \omega_1^\rho + \omega_2^\mu - \omega_3^\lambda, \\ \omega_1^\lambda + \omega_2^\rho - \omega_3^\mu, \ldots = \pm\tfrac{1}{4}, \pm\tfrac{3}{4}, \pm\tfrac{5}{4}, \ldots\}.$$

Note that $\omega_i^\mu + \omega_j^\lambda - \omega_k^\rho$ are the arguments of sines and cosines. Clearly, for such ω_i^μ the right-hand sides of (18*b*) are identically zero, and remain so for all t. Only the amplitudes R_i^μ then evolve dynamically by (18*a*), in which sine terms are ± 1. An interesting subset of $\mathscr{S}$ is

$$\mathscr{S}' = \{\text{arbitrary } R_i^\mu \text{ and } \omega_i^1 = \omega_i^2 \text{ such that} \\ \omega_1^1 + \omega_2^1 - \omega_3^1, \omega_1^1 + \omega_3^1 - \omega_4^1, \ldots = \pm\tfrac{1}{4}, \pm\tfrac{3}{4}, \pm\tfrac{5}{4}, \ldots\}.$$

Since $\omega_i^1 = \omega_i^2$, each of the terms $\sin 2\pi(\omega_i^1 - \omega_i^2)$ is zero, and remains so for all t. That is, $\mathscr{S}'$ is a submanifold of the phase space, independent of helicity, and hence is, perhaps, exceptional.

In § 5 we have already used the initial condition

$$I_{13} = \{R_i^\mu = \sqrt{\tfrac{1}{26}}, \omega_i^\mu = \tfrac{1}{8}\ (\mu = 1, 2;\ i = 1, 2, \ldots, 13)\},$$

which represents zero helicity ($H = 0$), for $\omega_i^1 = \omega_i^2$ at the initial time. By reversing the sign of ω_i^2 in I_{13}, we have

$$I'_{13} = \{R_i^\mu = \sqrt{\tfrac{1}{26}}, \omega_i^1 = -\omega_i^2 = \tfrac{1}{8}\ (\mu = 1, 2;\ i = 1, 2, \ldots, 13)\},$$

which, according to (7), represents the maximum helicity, since $|\sin 2\pi(\omega_i^1 - \omega_i^2)| = 1$. An intermediate helicity may be represented for instance by

$$I''_{13} = \{R_i^\mu = \sqrt{\tfrac{1}{26}}, \omega_i^1 = \tfrac{1}{8}, \omega_i^2 = 0 \quad (\mu = 1, 2;\ i = 1, 2, \ldots, 13)\}.$$

Our contention is that I_{13}, I'_{13} and I''_{13} can generate typical trajectories of zero helicity, maximum helicity, and an intermediate helicity, respectively (as will be discussed below under the heading *Sensitive dependence on the initial conditions*). Unlike energy and enstrophy of two-dimensional turbulence, which are interdependent, one may assign helicity quite arbitrarily (but between the zero and maximum values), independent of energy. For instance the zero helicity corresponds to isotropic turbulence; hence most of the numerical experiments to be reported below have been evolved from I_{13}. In an attempt to detect possible separation of the phase space into random and ordered regions (e.g. Hénon & Heiles 1964), we have tested other initial data besides I_{13} and I'_{13} and I''_{13}. However, no such separations have been observed. This conclusion is, at best, only tentative in that there are (infinitely) many other initial data yet to be tested.

A last comment before presenting numerical results is that overall (macroscopic) dynamics are not sensitive to the choice of ξ, except for $\xi = \frac{1}{4}$. It has been shown (Lee 1979) that $\xi = \frac{1}{4}$ imposes extraneous symmetries on the coupling coefficients, and hence will be excluded from further consideration. We shall therefore use one of

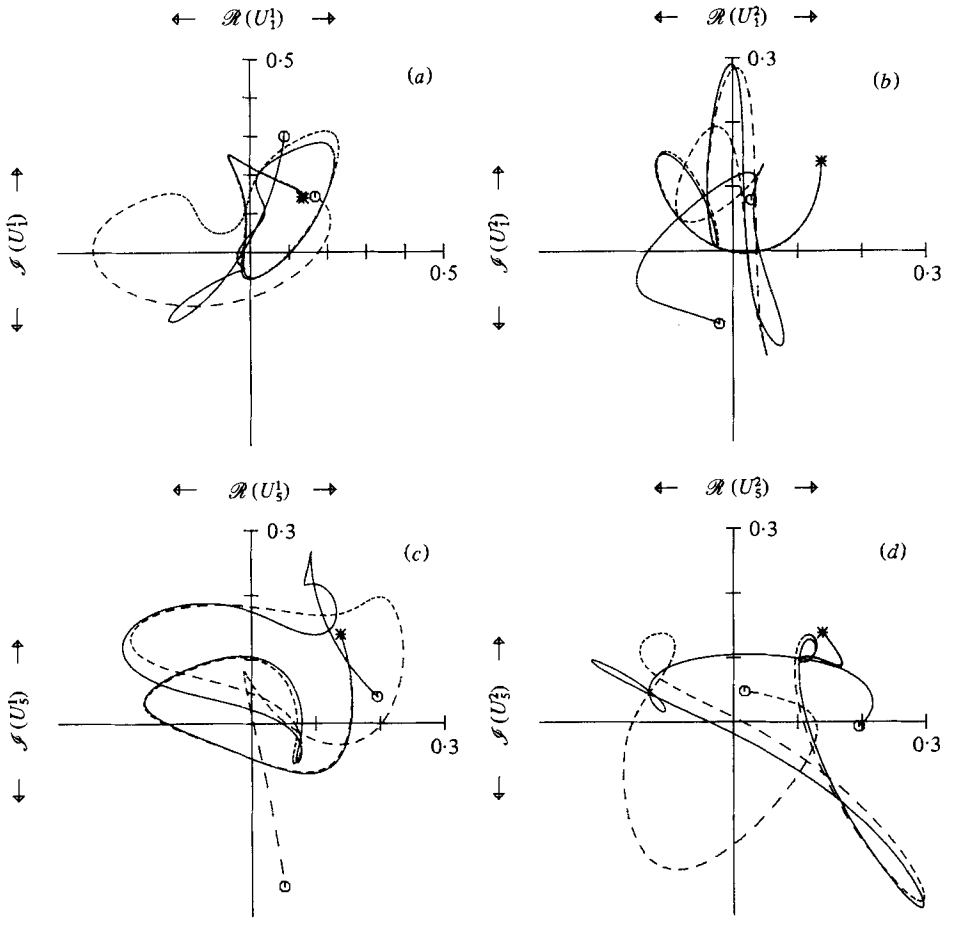

FIGURE 6. Exponential orbit separation of the (solid-lined) trajectory of $D(13, I_{13}, \frac{3}{8}, 0, 25)$ from the (dotted-lined) trajectory of $D(13, I_{13}''', \frac{3}{8}, 0, 25)$. ✳, initial point; ○, final point. Phase plots of (*a*) u_1^1; (*b*) u_1^2; (*c*) u_5^1; (*d*) u_5^2.

the four values $\xi = 0, \frac{3}{8}, \frac{2}{3}$ and 0·87654, more or less arbitrarily for the numerical results to be presented here.

Sensitive dependence on the initial conditions. Let us consider another initial condition

$$I_{13}''' = \{R_i^\mu = \sqrt{\tfrac{1}{26}},\ \omega_i^\mu = \tfrac{1}{8} + 0{\cdot}005\delta_{i,1}^{\mu,1} \quad (\mu = 1, 2;\ i = 1, 2, \ldots, 13)\},$$

which differs slightly only in the phase of u_1^1; otherwise it is completely identical with I_{13}. In figure 6 we have presented the simultaneous trajectories of $D(13, I_{13}, \frac{3}{8}, 0, 25)$ and $D(13, I_{13}''', \frac{3}{8}, 0, 25)$, which break away from each other in such a manner that, after a short time $T = 25$, they do not show any sign of the initial proximity in phase space. In other words, the divergence of initially nearby trajectories is completely unpredictable; hence the precise details of trajectory are quite sensitive to the initial conditions. However, when certain time averages are considered, random behaviour of the trajectory gets averaged out. This therefore permits us to use a single initial condition, such as I_{13}, to generate a generic trajectory, from which typical statistics may be computed, independently of the choice of initial data.

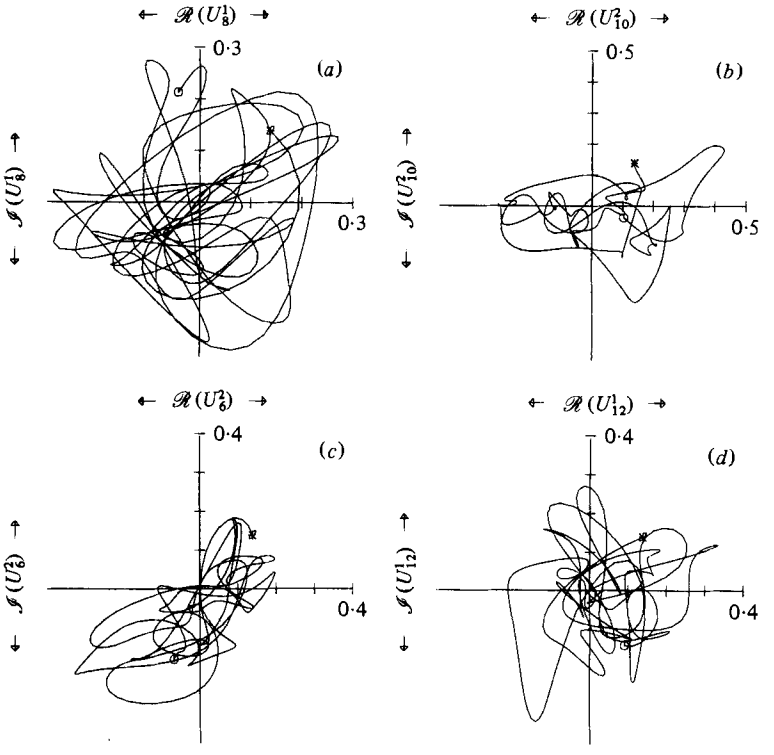

FIGURE 7. Random trajectory of $D(13, I_{13}, \frac{3}{8}, 0, 130)$. ✳, initial point; ○, final point. Phase plots of (*a*) u_8^1; (*b*) u_{10}^2; (*c*) u_6^2; (*d*) u_{12}^1.

Random trajectory. As was alluded to by the phase plots of figure 6, $D(13)$ develops apparently random trajectories. Figure 7 contains some typical phase plots of $D(13, I_{13}, \frac{3}{8}, 0, 130)$. The choice of $T = 130$ was made to match the evolution time of figure 12, which calls for an even longer evolution time for autocorrelation computations. Two observations are relevant here. First of all, the phase plots show no inaccessible annular region such as found in figures 6(*d–f*) of Lee (1979); hence the trajectory flow is apparently unconstrained in the phase space. Secondly, the phase plots in general tend to cover all four quadrants. In particular, the phase plot of figure 7(*a*) traverses the four quadrants more uniformly and randomly than the remaining figures 7(*b–d*). When $\mathscr{R}(u_i^\mu)$ and $\mathscr{I}(u_i^\mu)$ are considered as phase functions, uniformly and randomly traversing phase plots will satisfy the zero-mean condition (10). In this respect, we may say the trajectory of figure 7(*a*) obeys the zero-mean condition more faithfully than those of figures 7(*b–d*).

Ergodic behaviour of modal energies. We shall present here a limited test for ergodicity (8) by restricting the phase functions to be the modal energies J_i^μ. The reason for this choice of phase functions is that their phase averages have already been computed, based on the canonical distribution, which approximates the microcanonical distribution quite satisfactorily for the present system of 52 degrees of freedom. Recall the following result: energy equipartition (15) prevails under zero helicity, whereas in the non-zero helicity case the phase-averaged modal energies $\langle J_i^1 \rangle$ and $\langle J_i^2 \rangle$ have the same distribution (14*a*). We have presented in figures 8 and 9 the time-averaged

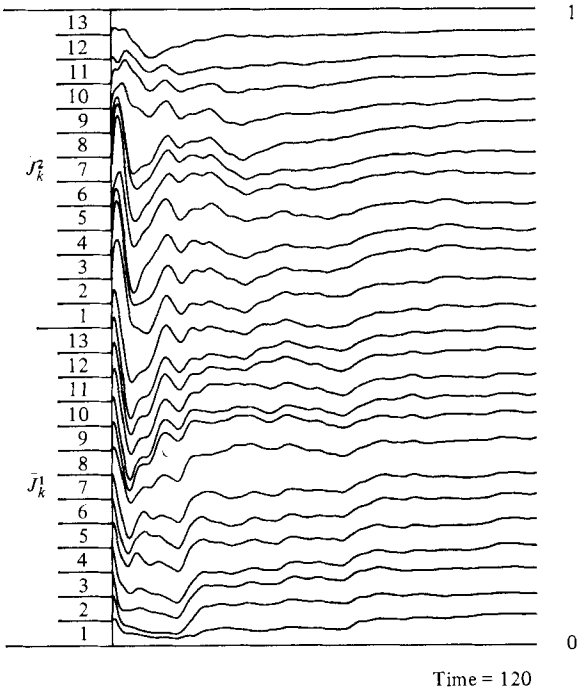

FIGURE 8. Time-averaged actions of $D(13, I_{13}, 0{\cdot}87\,654, 0, 120)$ representing zero helicity.

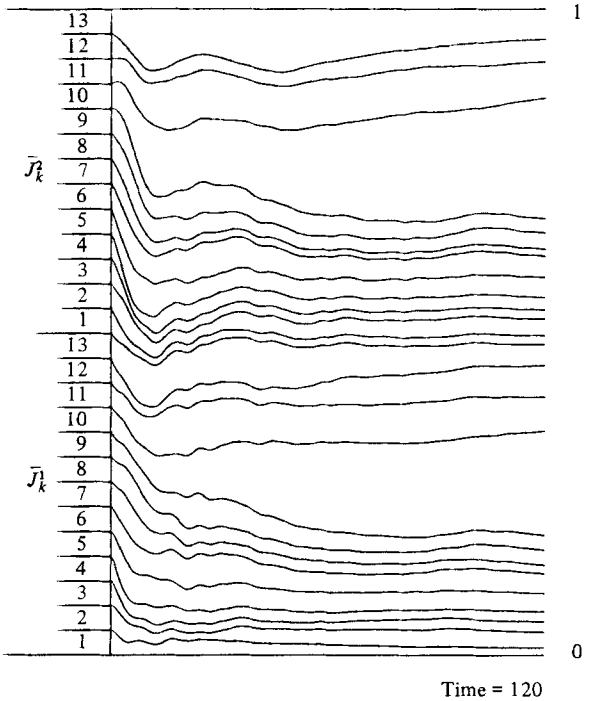

FIGURE 9. Time-averaged actions of $D(13, I'_{13}, 0{\cdot}87\,654, 0, 120)$ representing maximum helicity.

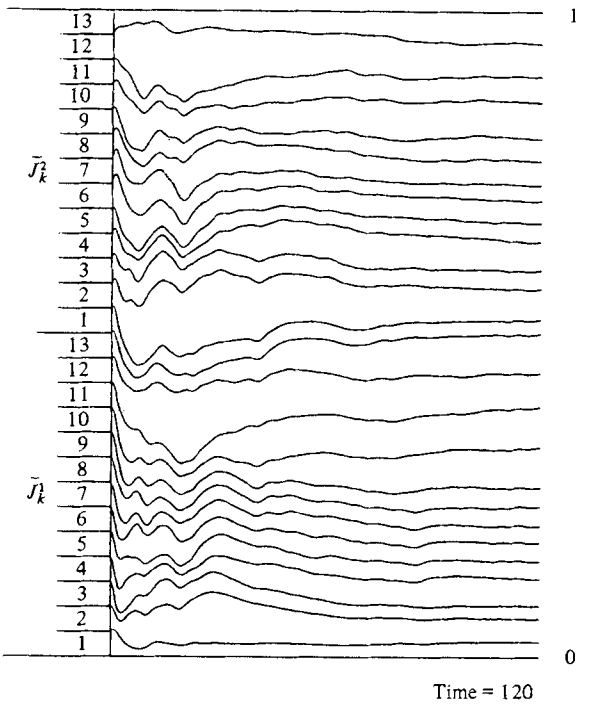

FIGURE 10. Time-averaged actions of $D(13, I''_{13}, 0{\cdot}87\,654, 0, 120)$ representing an intermediate helicity.

actions under the initial conditions I_{13} and I'_{13}, respectively. For zero helicity, figure 8 indicates a tendency towards energy equipartition. On the other hand, figure 9 depicts the equality of modal energy distributions under a maximum helicity. It is noted that figures 8 and 9 are intended for qualitative inference only. To be quantitative, we need to extend the evolution time much beyond $T = 120$, which we shall not do because the mixing property stronger than ergodicity will be demonstrated later on.

As mentioned in the beginning of this section, although extreme, the choice of zero and maximum helicity is not at all exceptional (non-generic). Theoretically this is evident from the equilibrium distribution (14), which depends continuously on C_1 and C_2. To lend a further numerical support, we have presented in figure 10 the time-averaged actions under an intermediate helicity. Note that qualitatively the long-time energy distribution lies somewhere in-between figures 8 and 9.

Decay of $\overline{U}_4$. Under energy equipartition, isotropy of the covariance spectral tensor calls for the disappearance of the real part of the reflectional asymmetry U_4, given by (16). The phase average $\langle U_4 \rangle$ based on the canonical distribution is identically zero (§ 4.7). We shall now compute its time average from the trajectory of $D(13, I_{13}, 0, 0, 120)$. As shown in figure 11, the asymptotic decay of $\overline{U}_4$ has been brought about by random oscillations of the time history of U_4.

Decay of autocorrelation functions. Under the ergodic assumption, let us compute the autocorrelation $\rho_i^\mu(T, \tau)$ for $\mathscr{R}(u_i^\mu)$ as defined by (12). (The correlations for $\mathscr{I}(u_i^\mu)$ will not be discussed here, for they exhibit more or less the same decay behaviour as $\rho_i^\mu(t, \tau)$.) Figure 12 presents autocorrelation functions computed from the same

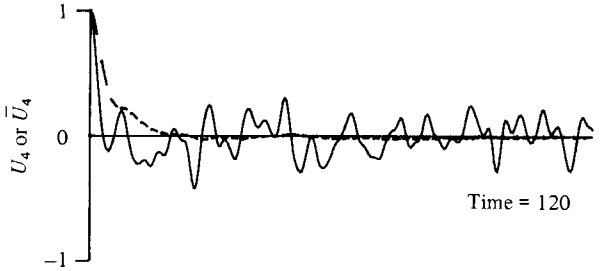

FIGURE 11. Evolution of the real part of the reflectional asymmetry of $D(13, I_{13}, 0, 0, 120)$. ——, U_3; - - -, $\bar{U}_4$.

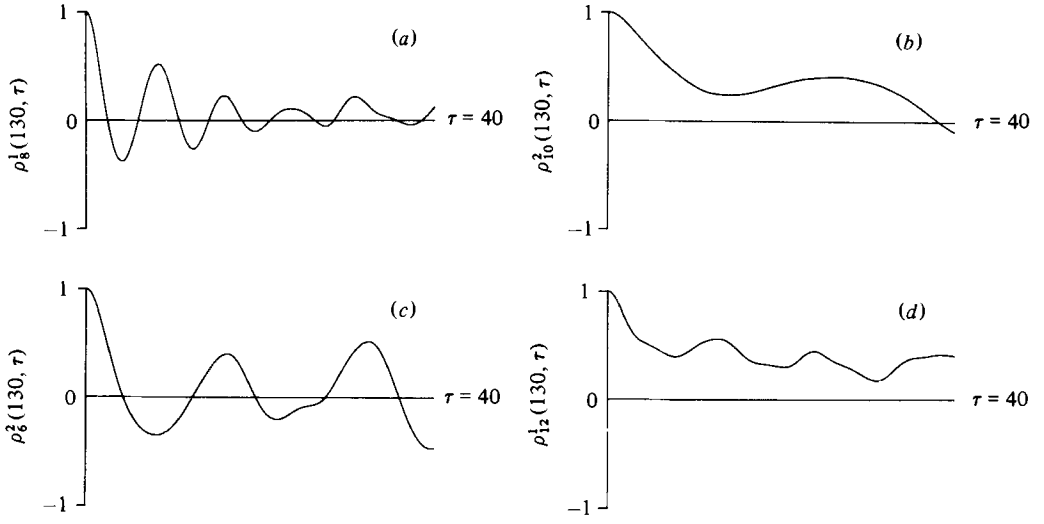

FIGURE 12. Autocorrelation functions generated from the trajectory of $D(13, I_{13}, \frac{3}{8}, 0, 130)$. Correlations of (*a*) $\mathscr{R}(u_8^1)$; (*b*) $\mathscr{R}(u_{10}^2)$; (*c*) $\mathscr{R}(u_6^2)$; (*d*) $\mathscr{R}(u_{12}^1)$.

trajectory as in figure 7. Figure 12(*a*) typifies the majority of ρ_i^μ, whereby correlation falls off rapidly and decays with damped oscillations. However, it would be misleading not to mention some anomalous cases, such as those depicted by figures 12(*b–d*). First of all, the correlation of figure 12(*b*) decays, but very gradually in the time range that ρ_8^1 has undergone several oscillations. That is, ρ_{10}^2 has a much longer correlation time than ρ_8^1. Secondly, the correlation of figure 12(*c*) falls off initially, but remains at a higher level even toward the end of τ. This is clearly a reflection of the somewhat mildly erratic trajectory of figure 7(*c*). Lastly, the correlation of figure 12(*d*) lies well above zero for the entire range of τ. We suspect this to be a consequence of the violation of the zero-mean condition (10).

Since the anomalies are due mainly to insufficient evolution time, we shall recompute figures 12(*b–d*), but with a much longer $T = 250$. Of course, the justification for computing autocorrelations from a pseudo-orbit is derived from the observation of Benettin *et al.* (1978) that the Anosov–Bowen theorem (§4.9) is applicable not only to Anosov systems, as originally intended, but also to some other systems (e.g. the Hénon–Heiles model) exhibiting chaos. The recomputed correlations are shown in figure 13. Note that figure 13(*a*) extends over $\tau = 150$ to permit development of

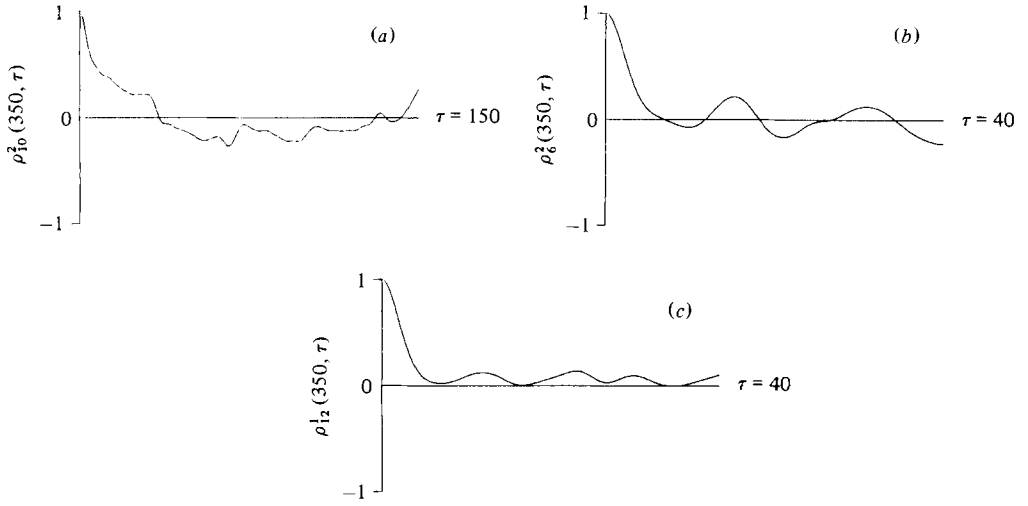

FIGURE 13. Autocorrelation functions generated from the trajectory of $D(13, I_{13}, \frac{3}{8}, 0, 350)$. Correlations of (*a*) $\mathscr{R}(u^2_{10})$; (*b*) $\mathscr{R}(u^2_6)$; (*c*) $\mathscr{R}(u^1_{12})$.

correlation over several correlation times. To a large degree, the anomalies of $\rho^\mu_i(130, \tau)$ have disappeared in $\rho^\mu_i(350, \tau)$, thereby indicating the mixing property of $D(13)$.

Kolmogorov entropy. The trajectory of $D(13, I_{13}, \frac{3}{8}, 0, 300)$ will be designated as the reference U of § 4.8. For the first time interval $(0, \Delta\tau)$, we evolve a neighbouring trajectory from the initial condition

$$I_0 = \{R^\mu_i = \sqrt{\tfrac{1}{26}},\ \omega^1_i = \omega^2_i = \tfrac{1}{8} + \Delta\omega \quad (\mu = 1, 2;\ i = 1, 2, \ldots, 13)\},$$

which represents a shift of all angles of I_{13} by $\Delta\omega$. Typically, we let $\Delta\omega = 0{\cdot}002$; hence the initial distance is $d = \|I_0 - I_{13}\| \simeq 0{\cdot}012\,566$. For the second time interval $(\Delta\tau, 2\Delta\tau)$ we shall specify the initial condition I_1 as follows. First note that each mode of I_0 is displaced from I_{13} by the same distance $[\frac{1}{13}(1 - \cos 2\pi\Delta\omega)]^{\frac{1}{2}}$. Consider U at $T = \Delta\tau$, and denote its real and imaginary components by $\tilde{v}^\mu_i$ and $\tilde{w}^\mu_i$, respectively. We then define each mode of I_1 by requiring that it has the same magnitude $[(\tilde{v}^\mu_i)^2 + (\tilde{w}^\mu_i)^2]^{\frac{1}{2}}$ as U at $T = \Delta\tau$, but its angle is shifted by

$$\frac{1}{2\pi}\arccos\left(1 - \frac{1 - \cos 2\pi\Delta\omega}{26[(\tilde{v}^\mu_i)^2 + (\tilde{w}^\mu_i)^2]}\right)$$

to maintain the same distance $[\frac{1}{13}(1 - \cos 2\pi\Delta\omega)]^{\frac{1}{2}}$. Then the distance of I_1 from U at $T = \Delta\tau$ would be exactly $d \simeq 0{\cdot}012\,566$. A similar procedure can be repeated for the initial condition I_2, and so on. Although there is nothing unique about our choice of initial conditions $I_1, I_2, \ldots$, the only justification is that the computed $k_n(\Delta\tau, U, d)$ are insensitive to $\Delta\omega$ (and hence d), as called for by condition (iii) of § 4.8. For instance, either by halving $\Delta\omega$ ($= 0{\cdot}001$) or reversing the direction of angle shift, the maximum deviation in $k_n(\Delta\tau, U, d)$ has been found to be less than 0·1 %.

Next, to check conditions (i) and (ii) of § 4.8, we have computed $k_n(\Delta\tau, U, d)$ under several values of $\Delta\tau$. One finds from figure 14 that $k_n(\Delta\tau, U, d)$ settle down to constant values of all $\Delta\tau$. Hence condition (i) is apparently satisfied. Yet the limiting values $k(\Delta\tau, U, d)$ are not the same, and thereby violate condition (ii). However, this is inevitable because the entropy computation is possible only for certain values of $\Delta\tau$.

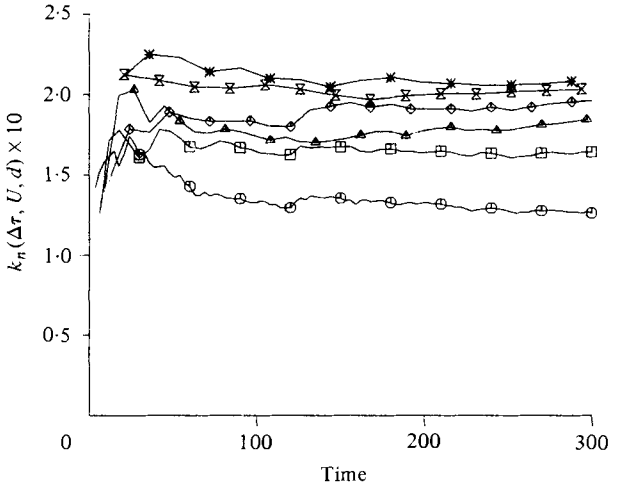

FIGURE 14. Kolmogorov entropy based on the reference trajectory $D(13, I_{13}, \frac{3}{8}, 0, 300)$. ⊙, $\Delta\tau = 3$; □, 6; △, 9; ◇, 12; ✳, 18; ⧖, 21.

That is, there are upper and lower limits for $\Delta\tau$. Note that the smallest time interval $\Delta\tau = 3$ in figure 14 is about half the typical correlation time estimated from figure 12(*a*). For $\Delta\tau < 3$, it has been found that some of the terms $\ln(d_j/d)$ become negative, so that $k_n(\Delta\tau, U, d)$ decrease steadily with increasing n. That is, nearby trajectories are actually being drawn in together, rather than breaking away from each other, in some time intervals. Since the decreasing $k_n(\Delta\tau, U, d)$ imply a non-random trajectory (Benettin *et al.* 1976), we may identify $\Delta\tau = 3$ as a threshold time for the apparent trajectory instability. Now, as $\Delta\tau$ (> 3) increases, so does $k(\Delta\tau, U, d)$, but at a gradually decelerating rate. For $\Delta\tau > 18$, however, one finds that a decreasing trend sets in, as indicated by $k(21, U, d)$ in figure 14. This is because the Euclidean metric (17) cannot discern different Riemann sheets, so that the trajectories with a shrinking distance (17) may indeed be diverging from each other when the angle variation is correctly taken into account.

In conclusion, the violation of condition (ii) is inevitable. It must, however, be noted that the computed $k(\Delta\tau, U, d)$ also depends on the reference trajectory U. Since the spread of $k(\Delta\tau, U, d)$ in figure 14 is well within its variation for different reference trajectories, we shall accept figure 14 as numerical evidence for positive Kolmogorov entropy. Hence, $D(13)$ may be said to be a K-system.

7. Towards mixing as the truncation order increases

Because of trajectory instability, it was not possible to evolve the true trajectory of $D(13)$ for $T \gg 110$ to provide a direct test for ergodicity and mixing. Yet the limited trajectory evolution was a sufficient manifestation of mixing in that trajectory instability has further led to positive Kolmogorov entropy, which is a stronger dynamical characterization than mixing. In § 5 the effective evolution time was adopted as a practical measure of limited evolution time. This has been motivated by the consideration that the effective evolution time is practically infinite in the absence of trajectory instability, whereas it is in the order of a typical characteristic correlation

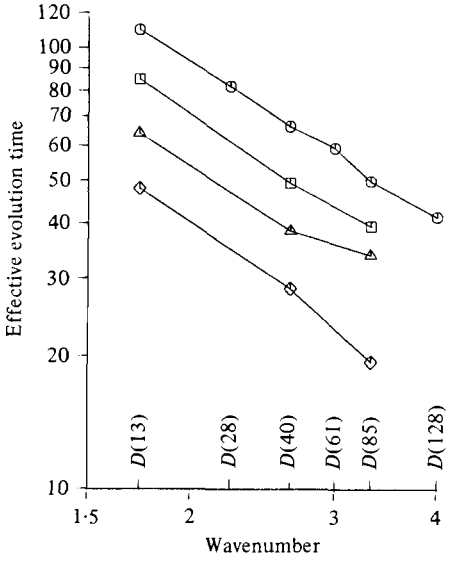

FIGURE 15. Effective evolution time determined from the forward–backward time integration of $D(N)$ under $\xi = \frac{3}{8}$ and I_N. ⊙, ABSERR = 10^{-13}; □, 10^{-11}; △, 10^{-9}; ◇, 10^{-7}.

time when the system is mixing. However, it is well known (Monin & Yaglom 1975, p. 340) that in fully developed turbulence the characteristic time scale of a typical eddy decreases with decreasing eddy size (increasing wavenumber). One therefore expects that the effective evolution time should decrease with increasing N, if the truncated system $D(N)$ exhibits enhanced mixing, as more and more triad interactions are included. To test this numerically we have carried out the forward–backward time integration of $D(N)$ for five values of N beyond $N = 13$ to determine effective evolution times based on the $\pm 0{\cdot}75\,\%$ recovery criterion set forth in § 5. Figure 15 summarizes the results of forward–backward time integration under the same parameter $\xi = \frac{3}{8}$ and initial condition I_N as in figure 3. The effective evolution time under ABSERR = 10^{-13} is denoted by ⊙ in figure 15. The decreasing trend of the figure is a macroscopic indication of tendency towards mixing as increasingly many triad interactions are included in $D(N)$. In the limit as $N \to \infty$, the effective evolution time will be in the order of the eddy-circulation time of the smallest eddy, which however decreases without bound in the inviscid case. Hence the inviscid flow becomes virtually uncomputable. This has been demonstrated explicitly in a Burger's model (Lee 1980).

Also included in figure 15 are the effective evolution times of $D(N)$ under less-stringent error tolerance ABSERR = 10^{-11}, 10^{-9} and 10^{-7}. Two things are noteworthy. First, the effective evolution time falls off with increasing N under all ABSERRs. Secondly, for a fixed order of truncation, the effective evolution time decreases significantly with increasing ABSERR. Based on the estimate of table 2, the computing cost can be more than halved by relaxing the ABSERR by two orders of magnitude. Therefore, although tempting to use a larger ABSERR for the sake of computing economy, one should be aware of the price paid for in terms of a smaller effective evolution time.

In conclusion, we have shown that the effective evolution time decreases monotonically with increasing order of spherical truncation. Hence the Navier–Stokes system

develops mixing on the constant-helicity surface, as we have speculated from the consideration of constants of motion.

The referee's reports have been invaluably helpful in the presentation of this paper. Their comments have in fact resulted in a complete overhaul of the original manuscript with the inclusion of a new theory section 4 to differentiate clearly the proven facts from numerical conjectures. I also wish to thank my colleagues Don Clemm, Paul Nikolai and Dennis Quinn for their help in overcoming numerous programming problems. Finally, correspondence with Dr L. Shampine should also be acknowledged.

Appendix: the vorticity interpretation of $u^\mu(\mathbf{k}, t)$

The vorticity $\boldsymbol{\omega}(\mathbf{k})$ is related to $\mathbf{U}(\mathbf{k})$ by the definition (omitting the factor i)

$$\boldsymbol{\omega}(\mathbf{k}) = \mathbf{k} \times \mathbf{U}(\mathbf{k}). \tag{A 1}$$

Because of the incompressibility $\mathbf{k}.\mathbf{U}(\mathbf{k}) = 0$, $\mathbf{k}$, $\mathbf{U}(\mathbf{k})$ and $\boldsymbol{\omega}(\mathbf{k})$ form a set of right-handed orthogonal vectors. Hence solving (A 1) for $\mathbf{U}(\mathbf{k})$ gives $\mathbf{U}(\mathbf{k}) = \boldsymbol{\omega}(\mathbf{k}) \times \mathbf{k}$, which in detail is

$$\mathbf{U}(\mathbf{k}) = \begin{pmatrix} 0 \\ -k_3 \\ k_2 \end{pmatrix} \omega_1(\mathbf{k}) + \begin{pmatrix} k_3 \\ 0 \\ -k_1 \end{pmatrix} \omega_2(\mathbf{k}) + \begin{pmatrix} -k_2 \\ k_1 \\ 0 \end{pmatrix} \omega_3(\mathbf{k}).$$

Since the three column vectors are all orthogonal to $\mathbf{k}$, one of them must be linearly dependent. Let us then eliminate the superfluous one, say the first column vector $(0, -k_3, k_2)$, with the use of $\mathbf{k}.\boldsymbol{\omega}(\mathbf{k}) = 0$ to give

$$\mathbf{U}(\mathbf{k}) = \mathbf{c}^2\omega_2(\mathbf{k}) + \mathbf{c}^3\omega_3(\mathbf{k}). \tag{A 2}$$

Here the column vectors $\mathbf{c}^2 = (k_3, k_2k_3/k_1, -k'^2/k_1)$ (where $k'^2 = k_1^2 + k_2^2$) and

$$\mathbf{c}^3 = (-k^2, (k_1^2 + k_3^2)/k_1, -k_2k_3/k_1)$$

are independent but not orthogonal. One may then take $\mathbf{k}$ and

$$\mathbf{c}^2/c^2 = (k_1k_3/kk', k_2k_3/kk', -k'/k) \equiv \mathbf{e}^2$$

as the two basis vectors and find the third (by the Gram–Schmidt procedure), which is $\mathbf{e}^1 = (-k_2/k', k_1/k', 0)$. Spanning by the new vectors $\mathbf{e}^1$ and $\mathbf{e}^2$, (A 2) becomes

$$\mathbf{U}(\mathbf{k}) = \mathbf{e}^1\omega^1(\mathbf{k}) + \mathbf{e}^2\omega^2(\mathbf{k}), \tag{A 3}$$

where $\omega^1(\mathbf{k}) = (k^2/k')\,\omega_3(\mathbf{k})$ and $\omega^2(\mathbf{k}) = (kk'/k_1)\,\omega_2(\mathbf{k}) + (kk_2k_3/k_1k')\,\omega_3(\mathbf{k})$. Since $\mathbf{e}^1$ and $\mathbf{e}^2$ are identical (except for the sign) with $\boldsymbol{\epsilon}^1(\mathbf{k}, 0)$ and $\boldsymbol{\epsilon}^2(\mathbf{k}, 0)$, respectively, we have shown that (A 3) is equivalent to the polarization-vector expansion (2) for $\xi = 0$. The new variables $u^\mu(\mathbf{k}, t)$ are, indeed, linear combinations of the vorticity components. Since $\mathbf{e}^1$ and $\mathbf{e}^2$ are but one of the infinite choices of basis vectors, the role of ξ is to parametrize this arbitrariness.

REFERENCES

Arnold, V. I. & Avez, A. 1968 *Ergodic Problems of Classical Mechanics.* Benjamin.
Bellman, R. 1953 *Stability Theory of Differential Equations.* McGraw-Hill.
Benettin, G., Galgani, L. & Strelcyn, J.-M. 1976 *Phys. Rev.* A **14**, 2338.

BENETTIN, G., CASARTELLI, M., GALGANI, L., GIORGILLI, A. & STRELCYN, J.-M. 1978 *Nuovo Cim.* **44B**, 183.

BIRKHOFF, G. & FISHER, J. 1959 *Rend. Circ. Mat. Palermo* **8**, 77.

BIRKHOFF, G. D. 1927 *Dynamical Systems.* Am. Math. Soc. Coll. Publ. vol. 9.

BRISSAUD, A., FRISCH, U., LÉORAT, J., LESIEUR, M. & MAZURE, A. 1973 *Phys. Fluids* **16**, 1366.

GLAZ, H. M. 1977 Statistical study of approximations to two dimensional inviscid turbulence. *Lawrence Berkeley Lab. Rep.* LBL-6708.

GLAZ, H. M. 1981 *SIAM J. Appl. Math.* **41**, 459.

HEMMER, P. C. 1959 Dynamic and stochastic types of motion in the linear chain. Thesis, Trondheim, Norway.

HÉNON, M. & HEILES, C. 1964 *Astron. J.* **69**, 73.

KELLS, L. C. & ORSZAG, S. A. 1978 *Phys. Fluids* **21**, 162.

KHINCHIN, A. I. 1949 *Mathematical Foundations of Statistical Mechanics.* Dover.

KRAICHNAN, R. H. 1973 *J. Fluid Mech.* **59**, 745.

LANFORD, O. E. 1976 *Qualitative and Statistical Theory of Dissipative Systems.* Lecture notes of 1976 CIME School of Statistical Mechanics.

LEBOWITZ, J. L. 1972 In *Statistical Mechanics: New Concepts, New Problems, New Applications* (ed. S. A. Rice, K. F. Freed & J. C. Light), p. 41. University of Chicago Press.

LEE, J. 1975 *J. Math. Phys.* **16**, 1367.

LEE, J. 1979 *Phys. Fluids* **22**, 40.

LEE, J. 1980 Emergence of periodic and nonperiodic motions in a Burgers' channel flow model. In *Proc. Int. Conf. on Nonlinear Phenomena in Mathematical Sciences, University of Texas at Arlington, June* 1980.

LEE, J. 1982 *Phys. Fluids* (to appear).

LEE, T. D. 1952 *Quart. Appl. Math.* **10**, 69.

LEITH, C. E. 1978 *Ann. Rev. Fluid Mech.* **10**, 107.

LIEPMANN, H. W. 1979 *Am. Scientist* **67**, 221.

LORENZ, E. N. 1969 *Tellus* **21**, 289.

MCLAUGHLIN, J. 1976 *J. Stat. Phys.* **15**, 307.

MONIN, A. S. & YAGLOM, A. M. 1975 *Statistical Fluid Mechanics*, vol. 2. MIT Press.

NEMYTSKII, V. V. & STEPANOV, V. V. 1960 *Qualitative Theory of Differential Equations.* Princeton University Press.

ORSZAG, S. A. & PATTERSON, G. S. 1972 *Phys. Rev. Lett.* **28**, 76.

PRIGOGINE, I. 1979 *Astrophys. Space Sci.* **65**, 371.

ROBINSON, G. D. 1967 *Quart. J. R. Met. Soc.* **43**, 409.

RUELLE, D. 1979 *Ann. N.Y. Acad. Sci.* **316**, 408.

SHAMPINE, L. F. & GORDON, M. K. 1975 *Computer Solution of Ordinary Differential Equations.* Freeman.

SINAI, YA. G. 1973 In *The Boltzmann Equation – Theory and Applications* (*Acta Phys. Austriaca, Suppl.* X) (ed. E. G. D. Cohen & W. Thirring), p. 575. Springer.